Title
Structural Transitions in Materials at High Pressure

Author
Smart, Thomas

Publication Date
2020

Peer reviewed|Thesis/dissertation

Structural Transitions in Materials at High Pressure

By

Thomas James Smart

A dissertation submitted in partial satisfaction of the

requirements for the degree of

Doctor of Philosophy

in

Earth and Planetary Science

in the

Graduate Division

of the

University of California, Berkeley

Committee in charge:

Professor Raymond Jeanloz, Chair
Professor Douglas Dreger
Professor Norman Yao

Fall 2020

Structural Transitions in Materials at High Pressure

Thomas James Smart

Abstract

Structural Transitions in Materials at High Pressure
by
Thomas James Smart
Doctor of Philosophy in Earth and Planetary Science
University of California, Berkeley
Professor Raymond Jeanloz, Chair

Structural transition in materials represents one of the most profound changes materials can undergo at high pressure and are an important part of studying planetary interiors. A material's crystal (or non-crystalline) structure influences its physical properties, including conductivity, elasticity, density and compressibility, and thus changes to that structure have profound effects on those physical properties. Studying these structural transition gives us an understanding of materials under extreme and dynamic conditions, such as deep interiors of planets, and subducting ocean slabs.

I studied the insulator to metal transition of $PbCl_2$ and $SnCl_2$, structural analogs to high-pressure SiO_2. Both density functional theory and X-ray diffraction shows two displacive phase transitions in the chlorides, as they transition from 9-fold coordinated to 10 and 11-fold coordinated structures. Absorption-edge spectroscopy shows that the bandgaps of $PbCl_2$ and $SnCl_2$ decrease with pressure, and we observe discontinuous changes in band-gap with crystal structural-induced changes in coordination number, suggesting a connection between interatomic geometry and the metallicity of these chlorides.

By implementing new techniques for acoustic monitoring, I study the structural transitions resulting from crystalline instabilities in silicon and serpentine. In silicon, I implement a fiber optic based acoustic sensor to expand the possible frequency response for acoustic monitoring to > 100 MHz, providing orders of magnitude better frequency response than previous work. We compressed silicon to 17 GPa, discovering 3 new acoustically active phase transitions on compression and decompression. Emissions range in duration from 10^{-7}-10^{-3} seconds, with the number of emissions roughly following a power law, similar to crustal earthquakes. In serpentine we monitor acoustic emissions resulting from solid-state amorphization using a 4-sensor acoustic array to get a sense of focal mechanisms. We record acoustic emissions to 26 GPa and find no purely isotropic sources from any of our experiments, replicating findings from natural high-pressure seismicity and setting a new pressure record for determination of focal mechanisms in the laboratory. In both silicon and serpentine, repeating acoustic emissions provide evidence for a self-propagating, transformation-driven process.

Professor Raymond Jeanloz
Dissertation Committee Chair

Contents

Chapter 1: Introduction

In order to accurately model the deep interiors of planets we must understand the material properties of the minerals that compose those interiors. A given mineral, on the microscopic level, is composed of a geometric arrangement of atoms in a crystal structure. The precise arrangement is determined by the lowest energy structure at a given pressure and temperature [J.W, Christian (1975)]. Substantial rearrangement of this structure due to a shifting stress or temperature environment is classified as phase transformation and represents one of the most important pathways to altering the physical properties of the crystal. These properties include compressibility, brittleness, electrical conductivity, magnetic moment, and chemical bonding. Understanding these attributes on the microscopic scale allows for more complete characterization of planet-scale phenomena.

There are two basic types of phase transition I will be discussing in this thesis; those whose transformation are diffusion dominated, and non-diffusion or 'Martensitic' transformations (Fig 1.1). Diffusion dominated transformations are characterized by nucleation and growth of a new phase within an existing phase. The rate at which these transformations occur is dependent on the driving forces (e.g. stress environment, temperature) acting on the crystal and is limited by the rates of chemical-diffusion processes. In practice, this means that crystals undergoing diffusion dominated phase transition can remain in a metastable state for some time, until the appropriate pressure-temperature conditions are met and the transformation concludes. In contrast, Martensitic transformations are time-independent, occurring almost instantly (approximately the sound speed of the material) as the entire crystal shifts from one crystal structure to another. Martensitic transformations occur spontaneously once the stress and temperature environment reach a point at which the parent crystal structure is no longer stable. [J.W, Christian (1975)]

It should be noted that plastic deformations of the crystal lattice, such as those caused by shear stresses, help to catalyze phase transformation both in diffusion-dominated and Martensitic transitions. In these cases, deformed regions experience higher effective driving forces and a lower free-energy barrier between phases [J.W, Christian (1975), Levitas and Javanbahkt 2015]. However, if dislocations in the crystal lattice that characterize plastic deformation are too numerous, long-range order of the crystal lattice can be destroyed, resulting in solid-state amorphization of the crystal: a structural change distinct from Martensitic and diffusion dominated transformations. It is a misconception that amorphization can occur only during melting of a material; indeed solid-state amorphization occurs when temperatures are too *low*, such that equilibrium phase transformation is kinetically hindered. This phenomenon is commonly thought to be characteristic of dynamic loading, such as in quasi-isentropic compression experiments, or the formation of "diaplectic glass" in meteorite impacts [Gleason et al 2017, Zhao 2018]. In fact, several experiments document solid-state amorphization under static compression, especially when large amounts of shear stress are present [Kingma et al. 1993, Grocholski et al 2010, Levitas et al 2012].

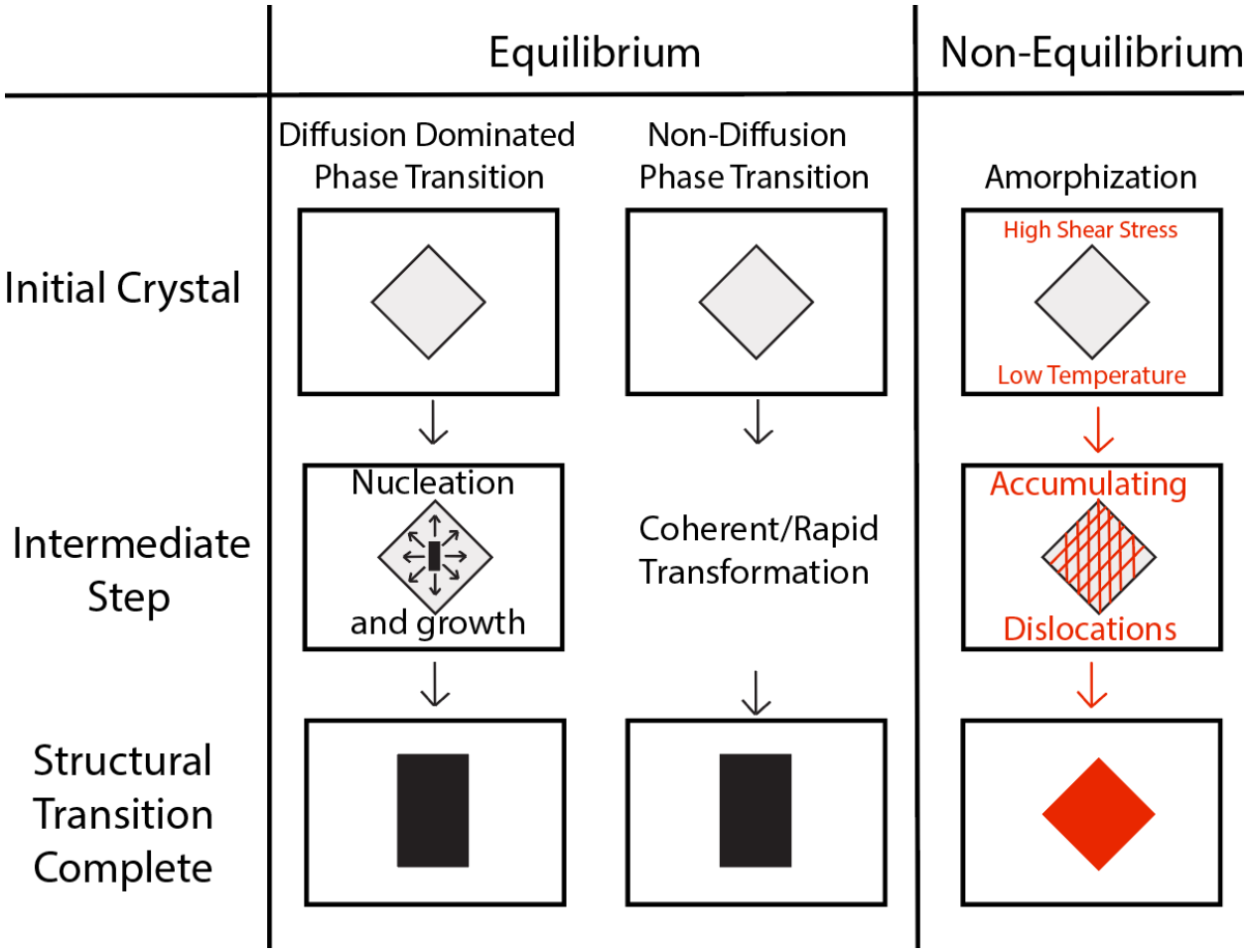

Figure 1.1. Schematic of different types of structural transitions**.** For the crystals in each diagram, grey represents the initial crystal phase, black represents the post-transformation crystal phase, and red represents dislocations in the crystal structure. Note that in the case of solid state amorphization, the amorphous material often retains the crystal habit (geometric shape) of the initial crystal but loses structural ordering.

Though the conditions under which structural transitions occur have been studied for many decades, investigating the details of these transitions can inform a wide variety of problems. This thesis is divided into two sections, each answering one of the following questions: how does a material's interatomic geometry effect its electrical conductivity, and how do acoustic emissions yielded during structural transition mimic high-pressure fracturing observed in nature?

The first section investigates the relationship between interatomic geometry of a compound and its metallicity. Several materials, including non-bonding noble gases, have been observed to metalize under compression, however the effects of atomic packing and interatomic geometry on the metallicity of a material are not well understood. [Stixrude and Jeanloz 2008, Celliers et al. 2010]. The majority of simple metals are observed to be 12-fold coordinated; that is, each of their atoms has 12 neighbors with whom they are bonded, so notionally, high coordination number is related to the metallicity condition [Pauling, 1960]. I investigate the insulator-to-metal transition in solid $PbCl_2$ and $SnCl_2$ from 9- to 11-fold coordination using combined x-ray diffraction to probe crystal geometry and absorption edge spectroscopy to measure metallicity. I find that metallicity in these compounds is determined by the combined

effect of bond angle straightening and increasing coordination number as each contribute to the overlapping of electron orbitals and therefore metallicity.

In the second section of the thesis, I investigate acoustic emissions yielded from materials at high pressure. Acoustic emissions at high pressure occur during rapid structural transitions (e.g. Martensitic transitions and amorphization), as shifts in the crystal structure change the material's volume and local stress environment, thereby releasing a pressure wave. These emissions resemble those yielded from brittle fracture at ambient conditions but persist to pressures and temperatures well beyond the expected 2-5 GPa brittle-ductile transition [Patterson and Wong 2005]. High-pressure acoustic emissions are interesting not only for revealing the nature of material failure at high pressures, but because high pressure fracture is also observed in nature during deep focus earthquakes, which have been observed to 700 km depth [Frohlich et al. 2006]. While the mechanism for high-pressure quakes has not been conclusively determined, instabilities catalyzed by structural transitions likely play a key role. While several studies have been conducted using acoustic emissions to draw conclusions about deep earth seismicity, they invariably have problems: their acoustic frequency response is too low to resolve length scales smaller than their entire pressure apparatus, and they often have peak pressures below 6 GPa, leaving the possibility that brittle fracture may be responsible for the emissions.

I observe the acoustic emissions in silicon and serpentine to pressures corresponding with deep focus earthquakes (>25 GPa). In Chapter 3, I use a fiber-optic sensor novel to high-pressure acoustic measurement, expanding the frequency response by 2 orders of magnitude (>100 MHz) and the sensor sensitivity by 3 orders of magnitude. In Chapter 4, I implement a new acoustic sensor array to determine focal mechanisms at 26 GPa, representing a factor of 4 improvement in the peak pressure for focal mechanism determination. I find that, similar to deep focus earthquakes, the number of high-pressure emissions follows a power-law with emission magnitude [Chapter 3] and has no purely-volumetric components to their focal mechanisms, mimicking focal mechanisms from deep focus earthquakes [Chapter 4]. In both experiments successive acoustic emissions suggest a self-catalyzing or 'domino-like' effect, in which local changes in stress environment caused by one acoustic emission can assist neighboring patches of material to overcome kinetic barriers and undergo structural transition.

References

J.W. Christian, *the Theory of transformation in Metal and Alloys Part 1: Equilibrium and General Kinetic theory, 2nd Edition*. Pergamon Press, 1975.

V. I. Levitas, M. Javanbakht, Interaction between phase transformation and dislocations at the nanoscale. Part 1 general phase field approach, Journal of the Mechanics and Physics of Solids 82, 287-319 (2015)

A.E. Gleason, C.A. Bolme, H.J. Lee, B. Nagler, E. Galtier, R.G. Kraus, R. Sandberg,W. Yang, F. Langenhorst, W. L. Mao, Time-resolved diffraction of shock-released SiO_2 and diaplectic glass formation. Nature communications 8:1481 (2017)

S. Zhao, R. Flanagan, E.N. Hahn, B. Kad, B.A. Remington, C.E. Wehrenberg, R. Cauble, K. More, M.A. Meyers shock induced amorphization in silicon carbide, Acta Materialia 158, 206-213 (2018)

K.J. Kingma, C. Meade, R.J. Hemley, H. Mao, D. R. Veblen. Microstructural observations of α-Quartz amorphization. Science 259, 666-669 (1993)

B. Grocholski, S. Speziale, R. Jeanloz, Equation of state, phase stability and amorphization of SnI_4 at high pressure and temperature. Physical Review B 81, 094101 (2010)

V. I. Levitas, Y. Z. Ma, E. Selvi, J. Z. Wu, J. A. Patten, High-density amorphous phase of silicon carbide obtained under large plastic shear and high pressure. Physical Review B 85, 5 (2012).

L. Stixrude and R. Jeanloz, Fluid helium at conditions of giant planet interiors, Proceedings of the National Academy of Sciences of the United States of America 105, 11071 (2008).

P. M. Celliers, P. Loubeyre, J. H. Eggert, S. Brygoo, R. S. McWilliams, D. G. Hicks, T. R. Boehly, R. Jeanloz and G.W. Collins, Insulator-to-Conducting Transition in Dense Fluid Helium, Physical Review Letters 104, 184503 (2010).
L. Pauling, *the Nature of the Chemical Bond, and the Structure of Molecules and Crystals: An Introduction of Modern Structural Chemistry,* 3rd Edition, Cornel University Press, 1960

M. S. Paterson and T.-F. Wong, *Experimental Rock Deformation – The Brittle Field*, 2nd Ed.(Springer, New York, 2005) pp 211-237.

T. J. Smart, E. F. O'Bannon III, M. R. Diamond, S. Stackhouse, B. K. Godwal, Q. Williams, and R. Jeanloz, Equation of state, phase transitions, and band-gap closure in $PbCl_2$ and $SnCl_2$: a joint experimental and theoretical study, Submitted for review at Physical Review B

T. Smart, H. Li, B. Dong, X. Shu, R. Hai, C. Sun, H.F. Zhang and R. Jeanloz, High-Pressure Nano-Seismology:
Use of Micro-Ring Resonators for Characterizing Acoustic Emissions, Applied Physics Letters 115, 3 (2019).

T. Smart, J. Parker, A. Ravid, S. Glaser, R. Jeanloz, Nano-Seismic Shear Sources from Serpentine at Lower mantle Pressures, Ch. 4, this Thesis.

Chapter 2:

Equation of state, phase transitions, and band-gap closure in $PbCl_2$ and $SnCl_2$: a joint experimental and theoretical study

The equations of state and band gap closures for $PbCl_2$ and $SnCl_2$ were studied using both experimental and theoretical methods. We measured the volume of both materials to a maximum pressure of 70 GPa using synchrotron-based angle dispersive powder X-ray diffraction. The lattice parameters for both compounds showed anomalous changes between 16-32 GPa, providing evidence of a phase transition from the cotunnite structure to the related Co_2Si structure, in contrast to the post-cotunnite structure as previously suggested. First principles calculations confirm this finding and predict a second phase transition to a Co_2Si-like structure between 75-110 GPa in $PbCl_2$ and 60-75 GPa in $SnCl_2$. Band gaps were measured under compression to ~70 GPa for $PbCl_2$ and ~66 GPa for $SnCl_2$ and calculated up to 200 GPa for $PbCl_2$ and 120 GPa for $SnCl_2$. We find an excellent agreement between our experimental and theoretical results when using the HSE06 hybrid functional, which suggests that this functional could reliably be used to calculate the band gap of other AX_2 compounds. Experimental and calculated band gap results show discontinuous decreases in the band gap corresponding to phase changes to higher coordinated crystal structures, giving insight into the relationship between interatomic geometry and metallicity.
Keywords: High Pressure, AX_2 compounds, $SnCl_2$, $PbCl_2$, Metallization

INTRODUCTION

The transition from insulating to metallic states is one of the most profound changes observed in high pressure science. Compression transforms materials to the metallic state by way of both classical (electrostatic repulsion) and quantum (Pauli exclusion) effects favoring delocalized electron states with increased density [1, 2]. However, it is unclear how changing local atomic-packing structure (e.g., coordination number) affects metallicity, as a material transforms to more highly coordinated structures under compression. Nevertheless, we recognize that most simple metals crystallize in close-packed structures (coordination number = 12) at ambient conditions [3].

Numerous studies of insulator-to-metal transitions under pressure have focused on the AX_2 family of compounds, which draw interest from a range of fields due to their planetary and technological importance and high diversity in bonding character; these materials include SiO_2, the archetype rock-forming compound, and its analogs. Recent experiments characterize AX_2 compounds (e.g., SiO_2, CaF_2) under dynamic compression, in which elevated temperatures melt the sample prior to metallization [4, 5]. It is perhaps revealing that the nearest-neighbor coordination number in at least some of these compounds (SiO_2, $AuGa_2$) increases under compression while in the fluid state, much as with crystal-structural phase transitions [6-8]. The

short time scales and fluid samples make typical methods of quantifying the interatomic geometry (e.g., X-ray diffraction) challenging, however.

Therefore, we use static high-pressure methods at 300 K to examine analogs of SiO_2 that already have highly coordinated cations at ambient conditions to document the relationship between band gap closure and interatomic geometry; specifically probing the key role of anion coordination in modulating band gaps under compression. Despite their diversity in bonding character, including halides, oxides, and intermetallics, AX_2 compounds typically follow a systematic sequence of high-pressure transformations, with materials with lower cation coordination number following similar phase-transition paths to higher coordination numbers (Fig. 2.1) [9-21]. The sequence of crystal structures is considered well-established up to the 9-fold coordinated cotunnite phase, the highest-coordinated AX_2 structure known at ambient conditions. These AX_2 compounds having high cation coordination numbers at ambient conditions (e.g. $PbCl_2$ and $SnCl_2$) are thus considered analogs for the high-pressure behavior of lower-coordination compounds in this family, with particular attention to SiO_2 at extreme conditions, as its presence is expected in the deep interiors of giant (H_2 + He), "icy" (molecular species, along with H_2 and He), and large-terrestrial (e.g., "super-Earth") planets [4, 14, 16].

In this study, we characterize the crystal structures, equations of state, and band gaps of $PbCl_2$ and $SnCl_2$ to pressures of over 70 GPa and compare our measurements with the results of ab-initio electronic structure calculations. Given that metallization (e.g., band-gap closure) is notoriously challenging to predict using first-principles calculations, experiments can be used to check theory, which – to the degree that it is thereby validated –can provide fruitful predictions of material properties at pressure-temperature conditions that are not accessible with current experimental techniques [22, 23].

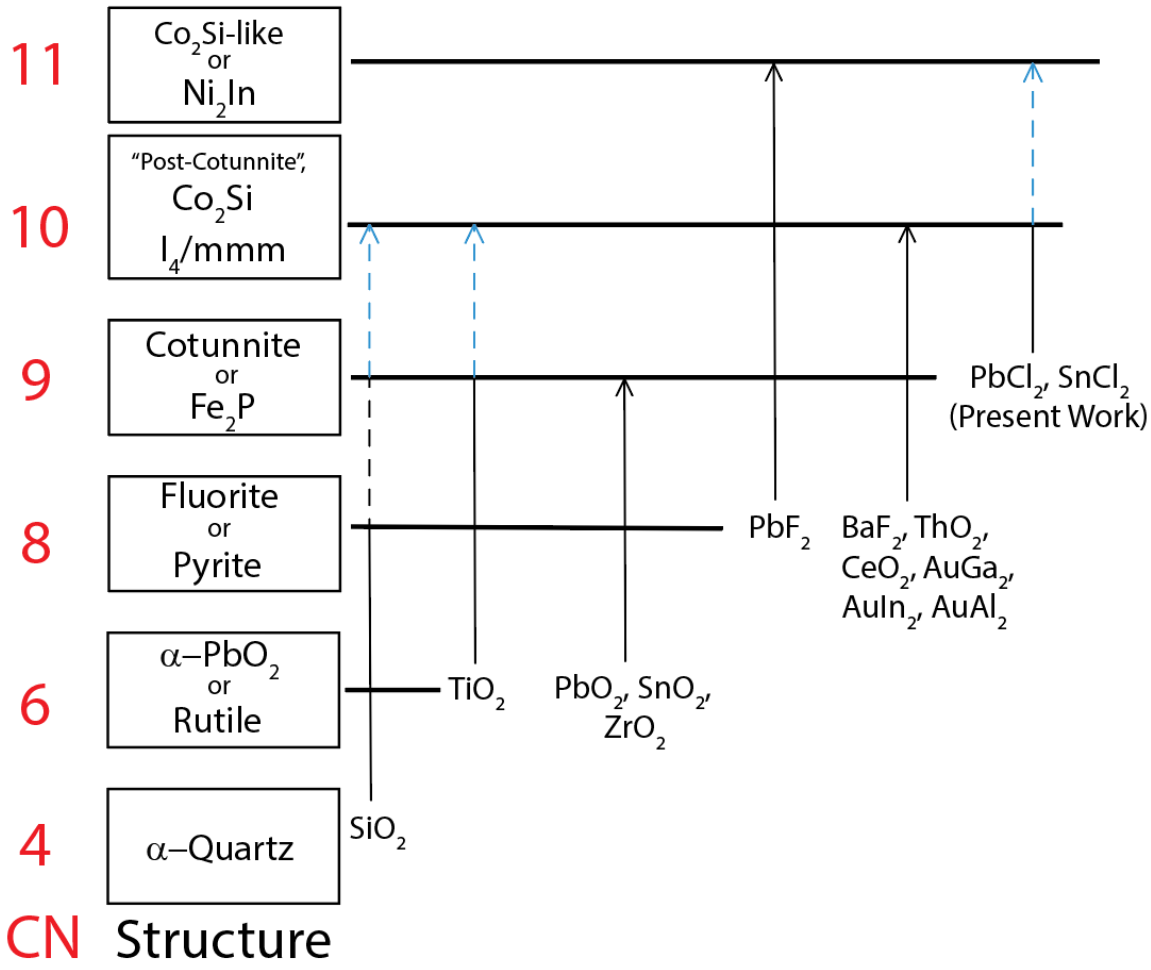

Figure 2.1. Crystal-structural sequence of AX_2 compounds at ambient conditions and high pressures. Figure after Leger et al. [9]. Cation coordination number (CN) of the cation is shown on the *left*, next to the structure name. Several AX_2 compounds are shown with *arrows* noting experimentally determined high-pressure phases [9-21]. *Dashed arrows* denote structures calculated from first principles, and *blue* color indicates that metallization is expected for the high-pressure phase. Several compounds (e.g., GeO_2, Na_2Te, HgF_2, $BaCl_2$, BaI_2, $BaBr_2$), and the effects of temperature are omitted for clarity.

METHODS

A. High-pressure experiments

Polycrystalline $PbCl_2$ and $SnCl_2$ (Sigma Aldrich >99% purity) were ground to micron-sized grains and loaded into symmetric-type diamond-anvil cells.Diamond anvils had a culet size of 200 μm, and rhenium gaskets pre-indented to ~30μm thickness and drilled with 80μm diameter holes were used. Ruby spheres of ≤ 5 μm diameter were placed inside the sample chamber and ruby fluorescence was used to determine the pressure [24]. All experiments were conducted at room temperature.

Samples were loaded in either a neon pressure medium, or a 16:3:1 methanol:ethanol:water pressure medium. $SnCl_2$ is hygroscopic, so it was loaded in a dry argon atmosphere. Mid-infrared spectra were collected to affirm minimal water content of $SnCl_2$ samples before all high-pressure experiments.

The band gap (absorption edge) was measured through visible and near-infrared spectroscopy. Optical absorption spectra were collected on a Horiba LabRam HR Evolution Raman spectrometer, with a white light source being used to collect spectra from 400-800 nm(3.1eV-1.55eV). Near-infrared spectra were collected using an evacuated Bruker Vertex 70v FTIR equipped with a tungsten source, InSb detector and CaF_2 beamsplitter [25]. Spectra were collected from 14,000 to 8,500 cm^{-1} (714.3 to 1,176.5 nm, 1.74 eV to 1.05 eV) with a resolution of 4 cm^{-1} (0.2-0.6 nm across this frequency range). No pressure medium was used in the experiments to measure the band gap under pressure, and the pressure gradients in these experiments are large. However, because of the spatial resolution of our instrument and the sharpness of the absorption edge of our samples, we do not anticipate that non-hydrostatic conditions adversely affect our band-gap determinations.

Angular dispersive synchrotron X-ray diffraction experiments were performed at beamline 12.2.2 at the Advanced Light Source (Lawrence Berkeley National Laboratory), using a monochromatic X-ray beam with $\lambda = 0.4959$ Å (25 keV). A Mar345 detector collected diffracted X-rays at 331.4 (±0.1) mm. Detector distance and orientation were calibrated using a LaB_6 standard, and the diffraction images were radially integrated using the programs FIT2D [26] or Dioptas [27].

We carried out Rietveld refinements using the General Structure Analysis System (GSAS) [28] Larson program, with starting atom positions chosen from the outputs of ab-initio density functional theory described in the following section. After fitting the background, the data were refined for lattice parameters. Pseudo-Voigt functions are used for the fitting of diffraction-peak profiles in the Rietveld refinements.

B. Theoretical Calculations

All calculations were performed using the density functional theory-based VASP code, employing the projector augmented-wave method [28-32]. The potentials were generated using valence configurations of $4d^{10}\ 5s^2\ 5p^2$ for Sn, $5d^{10}\ 6s^2\ 6p^2$ for Pb, and $3s^2\ 3p^5$ for Cl. Scalar relativistic effects were accounted for. However, spin-orbit coupling was only included in the calculations for $PbCl_2$ phases because it was found to have a negligible effect on the results of calculations for $SnCl_2$ phases. Computations were performed using both the local-density approximation (LDA) and Perdew-Burke-Ernzerhof (PBE) formulation of the generalized gradient approximation (GGA) [33, 34]. The LDA and GGA give reasonable estimates of structural parameters, but underestimate band gaps (e.g., Xiao et al., 2011) [35], due to their inherently incomplete cancellation of self-interaction [22, 23]. In view of this, additional band-gap calculations were performed using the Heyd-Scuseria-Ernzerhof (HSE06) hybrid functional, which incorporates a fraction of exact-exchange to alleviate the self-interaction error, on structures optimized using the PBE functional [36]. The HSE06 hybrid functional predicts band gaps that are in much better agreement with experimental measurements, but has a high computational cost, making it unsuitable for geometry optimizations in the present work [35, 37]. HSE06 was chosen out of the popular hybrid density functionals, because it is shown to be the most accurate in calculating the band gaps of semiconductors [37].

For geometry optimization calculations, the kinetic-energy cut-off for the plane-wave expansion was 600 eV, and Brillouin-zone sampling was performed using a 6×4×8 *k*-point grid [38]. These settings ensured calculated volumes were converged to within 0.05 $Å^3$, and enthalpies to within 1 meV per atom.

For LDA and PBE band-gap calculations, the kinetic-energy cut-off for the plane-wave expansion was 600 eV, and Brillouin-zone sampling was performed using an 11×7×15 *k*-point grid [38]. These settings ensured that calculated band gaps were converged to within about 0.05 eV or less. Due to the high computational cost associated with hybrid functional calculations, for HSE06 band gap and density of states calculations, Brillouin-zone sampling was performed using a 5×3×7 *k*-point grid [38]. Convergence tests for LDA and PBE suggest that using this smaller *k*-point grid leads to overestimates of the band gap of up to 0.05 eV for $SnCl_2$ and 0.2 eV for $PbCl_2$.

It is well known that LDA underestimates pressure, and PBE overestimates pressure. Because of this, a pressure correction was estimated using the method of Oganov et al. [39], but without a thermal pressure term (this is likely negligible at ambient temperature for these calculations performed at 0K). The calculated pressure shifts ($PbCl_2$: +2 GPa (LDA), - 2 GPa (PBE); $SnCl_2$: +2 GPa (LDA), - 1 GPa (PBE)) move the isothermal compression curves to higher or lower pressure, bringing them in better accord with experimental values.

RESULTS AND DISCUSSION

A. X-ray diffraction results

X-ray diffraction data were collected on compression and decompression to 71 GPa in both $PbCl_2$ and $SnCl_2$ (Fig. 2.2). Rietveld refinements of the diffraction patterns for both compounds document an isosymmetric phase transition from the cotunnite structure (orthorhombic *Pnma*, 9-fold coordination) to the Co_2Si structure (orthorhombic *Pnma*, 10-fold coordination) between 17 and 35 GPa for $PbCl_2$ and 17 to 33 GPa for $SnCl_2$, supporting a prior theoretical prediction [40] (structural diagrams are shown in Fig. 4). These findings are consistent with structural transitions documented in other AX_2 compounds such as PbF_2, $BaCl_2$, and $BaBr_2$ [11, 15], and the gradual nature of the transition is fully compatible with the close topological relationship between the cotunnite structure and the Co_2Si structure [41].

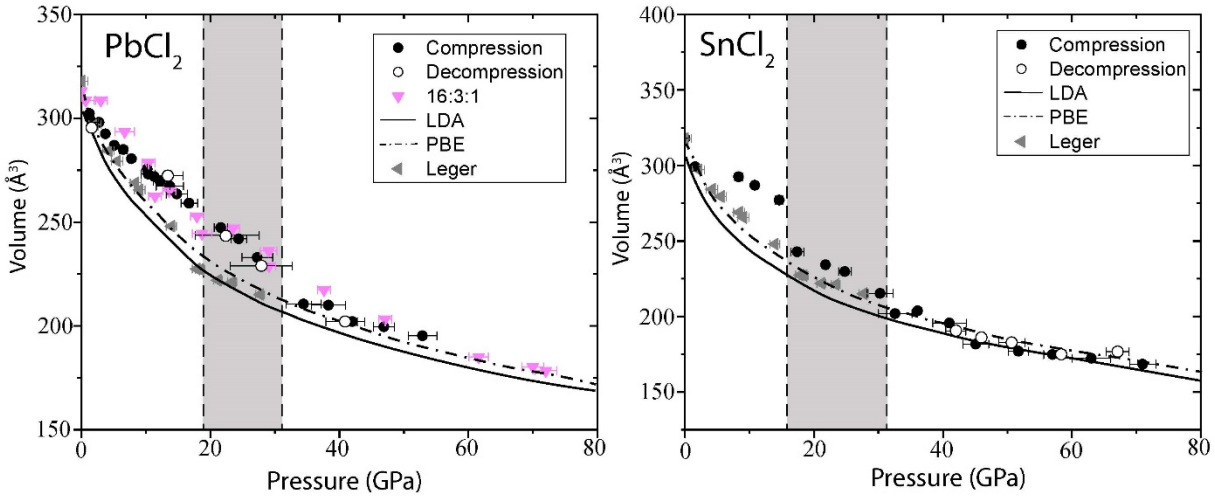

Figure 2.2. Pressure–volume data for $PbCl_2$ (*top*) and $SnCl_2$ (*bottom*). Data shown in *Black or hollow circles* were taken using neon pressure medium. *Pink triangles* not data taken using 16:3:1 methanol:ethanol:water pressure medium, and *grey triangles* are previous results from Leger et al. [12].The pressure-range for the transformation from cotunnite to Co_2Si structures, between 17 and 35 GPa for $PbCl_2$ and 17 and 33 GPa for $SnCl_2$, is shown by the *gray box* between *dashed lines* as it is for Figs. 2.3 and 2.6. Data collected on compression and decompression are distinguished by *closed* and *open circles*, respectively.

Measured lattice parameters provide a greater insight into the structural transition that occurs over a relatively large pressure range for both materials. The cotunnite-to-Co_2Si structural transition in these materials is characterized by an anomalous shift in relative length of lattice parameters (Fig. 2.3) [42]. This occurs between 17 and 35 GPa for $PbCl_2$ and between 17 and 33 GPa for $SnCl_2$. In these regions we observe anisotropic compressibility of the unit cell, with a strong compression along the *a-axis,* a reduced compression along *c-,* and *extension* along *b-, which has been reported to occur in other AX_2 compounds that transform from the cotunnite structure to the Co_2Si structure under compression (*e.g., PbF_2, CeO_2, and ThO_2) [15, 20]. While we were not able to collect data on decompression in the pressure range of this phase transition in $SnCl_2$, in $PbCl_2$ the transition is observed to be reversible with minor hysteresis.

The strong compression of the *a*-axis relative to the *b*- and *c*-axes is emphasized when we normalize the lattice parameters against their respective initial lengths (Fig. 3 c and d). The pressure range of the phase transition is marked by the gray shading between dashed lines, with a smooth transition in $PbCl_2$ that is complete by 33 GPa, and a sudden shift in $SnCl_2$ at 33 GPa. Due to the non-negligible pressure gradients, we attribute this more sudden shift between phases to be a result of non-hydrostatic stresses.

Previous experiments by Leger et al. [12] did not exhibit these continuous trends in lattice parameters or the presence of an intermediate phase and had strong hysteresis on decompression (gray triangles, Figs. 2.2 & 2.3). This difference is likely associated with the more non-hydrostatic stress environments within the samples of their experiments, as these had no pressure medium for $SnCl_2$ and silicone grease for $PbCl_2$. Because of the contrast in the nature of the transition (abrupt in the previous experiments and with an intermediate zone of transformation in ours), we do not preclude that the transition from the cotunnite to the Co_2Si structure can be driven/enhanced by non-hydrostatic stresses.

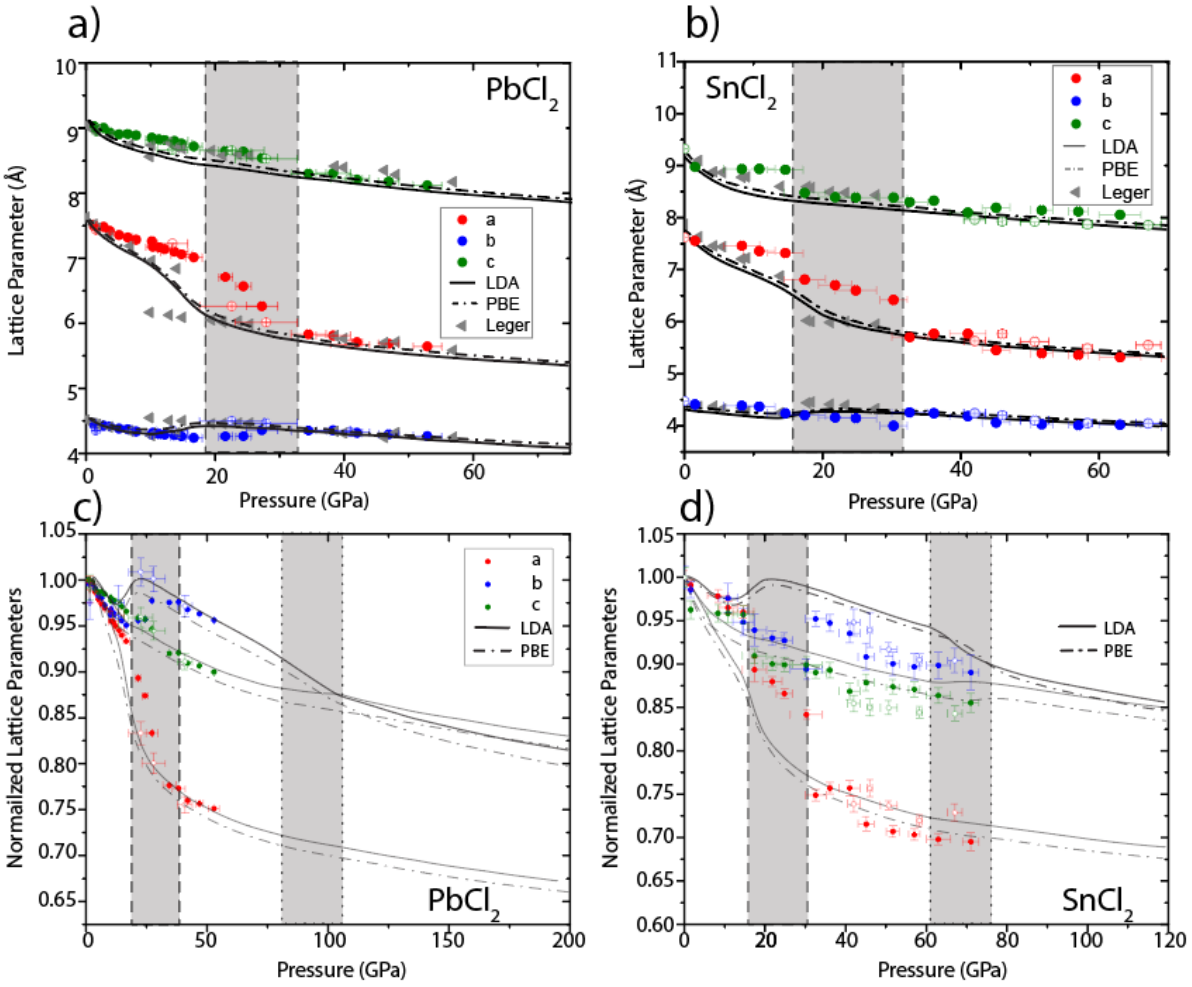

Figure 2.3. Lattice parameters vs. pressure from experiments and theory are presented for $PbCl_2$ (a) and $SnCl_2$ (b). Lattice parameters normalized against ambient-pressure values are presented as a function of pressure for $PbCl_2$ (c) and $SnCl_2$ (d). Lattice parameters show a gradual change in slope between 21 and 25 GPa for $PbCl_2$ and between 17 and 33 GPa for $SnCl_2$, contrasting with previous work that showed a sharp transition (*gray triangles* in a) and b)). We infer a gradual change in phase ("transition zone"), consistent with findings for other AX_2 compounds as the materials shift from the cotunnite to Co_2Si structure. We mark these transition zones with gray boxes, whose boundaries are defined by the observed shifts in lattice parameters (*gray boxes* with *dashed black lines*). The experimentally observed compression of the *a* and *c* axes and extension of the *b* axis is reflected in calculations. Upon further compression, LDA and PBE calculations predict a distortion of the Co_2Si lattice, seen here as a slight contraction of the *b* axis and extension of the *c* axis between 75 and 110 GPa in $PbCl_2$ and between 60 and 75 GPa in $SnCl_2$, shown by the *gray box* between *dotted lines* in c) and d).

Density functional theory calculations agree well with experimental data, with compression of the *a*-axis and extension of the *b*-axis reproduced by the calculations, albeit at pressures ~10 GPa lower than experimentally observed (Figs. 2.2 and 2.3). Between 75 and 110 GPa in $PbCl_2$ and 60 and 75 GPa in $SnCl_2$, PBE and LDA functionals predct another shift in structure from the 10-fold coordinated Co_2Si structure to an 11-fold coordinated Co_2Si-like phase (structure shown in Fig. 2.4). This phase shares the same space group as the Co_2Si structure (*Pnam*), but the rows of atoms become increasingly colinear and orthogonal to one another, as the anion sublattice begins to approach a close-packed array. The transition is characterized by a subtle extension of the *c*-axis and compression of the *b*-axis, which has pronounced expression in the normalized lattice parameters plots (Fig. 2.3 c and d, *gray shading* between *dotted lines*). As has been previously noted [14], the nine-fold cation coordination of the cotunnite structure is incompatible with close-packing of the anion framework. Indeed, the cotunnite structure can be

viewed as being comprised of interlinked $(MX_2)_n$ polymeric chains [43]. The sequential transitions can then be viewed as a progression from a phase characterized by high cation coordination but an inefficiently packed anion sublattice (anions coordinated in trigonal prisms) to a phase with both higher cation coordination and far more efficiently packed anions (Fig. 2.4 d). The transition sequence is a higher-coordination analogue to the structural shifts in the SiO_2-system at lower pressures, in which a polymeric low-pressure phase (quartz, with corner-linked SiO_4 tetrahedra) converts to the close-packed and more highly coordinated rutile structure.

Structural rearrangements from the cotunnite to Co_2Si and then to Co_2Si-like phases are shown in Fig. 2.4; the formation of new bonds between Pb or Sn and Cl is indicated by the *red* and *black arrows*. Electron density maps (Fig. 2.4 d) show that formation of the first bond (shown by the *red* and *black arrow*) occurs at 24 GPa in $PbCl_2$ and at 28 GPa in $SnCl_2$ (not shown), similar pressures to observations of analogous bonds forming in PbF_2 by Stan et al. [15]. Further compression leads to a tightly packed arrangement, with atoms forming an increasingly square lattice within each layer in the (010) plane, until the structure becomes 11-fold coordinated (Co_2Si-like structure) at 110 GPa in $PbCl_2$ and at 75 GPa in $SnCl_2$.

Reference	**Cotunnite structure**			**Co_2Si structure**			**Co_2Si-like structure**		
	V_0	**K_0**	**K_0'**	**V_0**	**K_0**	**K_0'**	**V_0**	**K_0**	**K_0'**
$PbCl_2$ This study	**313.06 ±0.05**	46.7±4.4	4.8±1.2	300(20)	47.2±3.2	4.0±1.0	281(27)	59.2±9.2	4.0±0
$SnCl_2$ This Study	**318.03 ±0.05**	27.9±2.1	6.3±0.5	292(43)	41.1±3.7	4.0±0.2	290(8)	43.7±0.1	4.0±0
$PbCl_2$ Ref. [12]	313.072	34±1	7.4±6	273.91	95±10	4.3±5			
$SnCl_2$ Ref. [12]	317.853	31±2	4.9±8	263.81	91±10	4.0*			

Table 2.1. Comparison of our equations of state with previous work by Leger et al. [12]. Zero-pressure volume V_0, bulk modulus K_0, and pressure derivative K_0' for the high-pressure phases (Co_2Si and Co_2Si-like) are determined through 3rd order Birch Murnaghan equations of state by fitting normalized pressure to Eulerian strain (G vs. g) [44] (see appendix B for details). The volume V_0 for the ambient pressure cotunnite phase is obtained from our X-ray diffraction data via Rietveld refinement and are fixed in these fits. *indicates values that were fixed in our fits (shown in Appendix B)

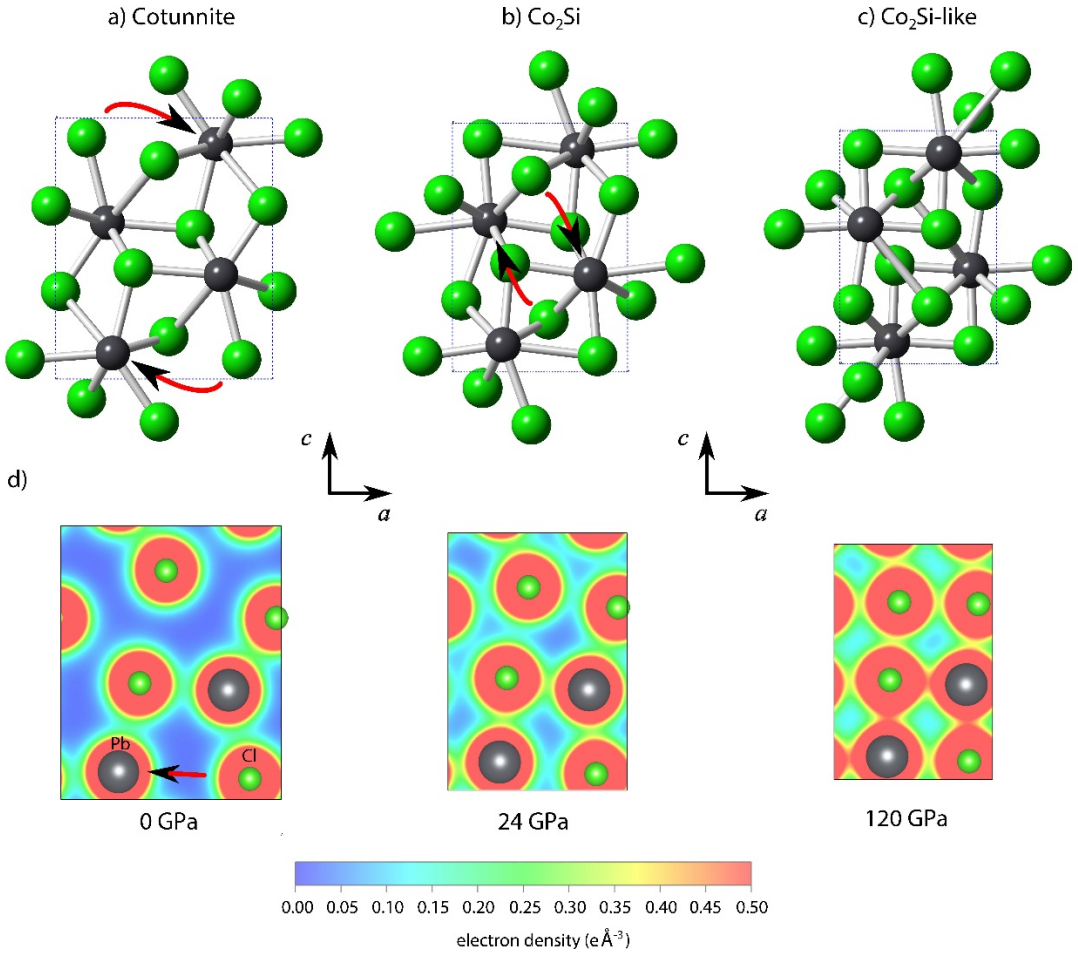

Figure 2.4. Structural diagrams of the cotunnite, Co_2Si, and Co_2Si-to-Co_2Si-like phases, with the Pb, Sn cations shown in *black* and chlorine shown in *green*. a), b), and c) show ball-and-stick models of the cotunnite, Co_2Si, and Co_2Si-like structures respectively, with *arrows* indicating the atomic motion that leads to new bonds in subsequent phases. d) shows the change in electron density in the (010) plane as a function of pressure. A new bond forms between Pb and Cl at 24 GPa, indicative of a transformation from the 9-fold coordinated cotunnite structure (a) to the 10-fold coordinated Co_2Si structure (b). For $SnCl_2$, formation of an analogous Sn-Cl bond is observed at about 28 GPa. On further compression the lattice continues to become more ideally packed, and new (Pb,Sn)-Cl bonds form. This Co_2Si-like structure is predicted by DFT to occur at 120 GPa in $PbCl_2$ and 80 GPa in $SnCl_2$. Figures were produced using VESTA 3 [45].

We fit our pressure-volume data with a 3rd order Birch-Murnaghan equation of state (EOS), and the obtained parameters are shown in Table 1. EOSs previously reported [12] were determined assuming a single phase, and we obtain similar results when we fit our data in this way. However, when we fit our high- and low-pressure phases separately, we find the high-pressure phase to have higher V_0 and lower bulk modulus K_0 than previously reported (fits shown in Appendix B).

B. Band-gap measurements

Representative absorption-edge spectra, collected between 30 and 70 GPa for $PbCl_2$ and between 20 and 66 GPa for $SnCl_2$, show good agreement with theory (Fig. 5 and Appendix D, Fig. 2.9). Of the three functionals used, as expected HSE06 agrees best with the experimental data, overestimating the band gap by only 0.2 eV, which is due to an incomplete convergence with respect to k-point sampling.

For $PbCl_2$ and $SnCl_2$ we observe three distinct regions in the theoretically calculated band gaps with compression. Discontinuities in the band gap vs. volume plots, and shallowing slope in the band gap vs. volume plots are attributed to changes in $PbCl_2$ and $SnCl_2$ as they transform from the cotunnite to Co_2Si phase (*gray box* with *dashed lines*) and from the Co_2Si to Co_2Si-like phase (*gray boxes* with *dotted lines*). Experimental data for $SnCl_2$ follow this trend, closely following values calculated by the HSE06 functional, at pressures and volumes coinciding with the calculated structural changes (Fig. 5 *b & d*).

When the experimental $PbCl_2$ data are extrapolated to zero band gap, we predict band closure at 206 ±24 GPa, which agrees with HSE06 calculated band-gap closure at 200 GPa. When we extrapolate the experimental $SnCl_2$ data for the Co_2Si-like phase (between 51 and 66 GPa) to zero band gap, we predict band closure at 125 ±9 GPa versus 120 GPa predicted by HSE06. If, however, we extrapolate the entire $SnCl_2$ experimental data set to zero band gap, we predict band closure at 97 (±6) GPa, representing a 20 GPa discrepancy between experiments and HSE06.

The lower metallization pressure of $SnCl_2$ relative to $PbCl_2$ differs from the typical trend of metallization pressures decreasing along isoelectronic series down the periodic table to heavier, more electron-rich compounds. This trend, which is also found in band-structure calculations of other compounds [46, 47], does not predict the relative band-gap closure pressures of the two compounds examined here. This apparent inversion of metallization pressure is likely generated by the relativistic down-shift and associated localization of the 6*s* lone pair in Pb relative to the somewhat more delocalized 5*s* lone pair in Sn. Indeed, portions of the Pb 6*s* states are among the deepest in the valence band at all pressures, and the 5*s* states of Sn systematically contribute substantially more to the density of states at the top of the valence band relative to the 6*s* states in $PbCl_2$ (see Appendix E). Comparable lowering of the band gap of SnO relative to PbO via this "inert lone pair" has been extensively documented at ambient pressures [48, 49], and we demonstrate here that this 6*s*-localization persists to high pressures in the chlorides of these elements.

We observe a dramatic increase in slope in the band gap vs. volume plot at high compression (Fig. 2.5, *bottom panels*). During compression of the initial cotunnite phase in both compounds, we observe a small reduction in band energy predicted by HSE06 calculations (5% and 14% of ambient pressure band gap for $PbCl_2$ and $SnCl_2$ respectively), despite a significant change in unit-cell volume (roughly 50% of the total volume closure of the materials, with total volume closure $V_{tot}= V_0-V_{band\ closure}$). At the onset of the transition between 9-fold coordinated cotunnite and 10-fold coordinated Co_2Si structures, we observe a large (>20%) reduction in the band gap in both compounds, despite small reductions in unit cell volume (~14% of V_{tot}). This transition is also accompanied by a shift in the cation coordination around the anions, from 4 and 5 for the two different Cl sites in the cotunnite structure toward 5 and 6 in the Co_2Si structure (as illustrated by the new Pb-Cl bond formation in Fig. 4). Upon further compression in the Co_2Si region, the slope becomes steeper, with small changes in the unit cell volumes (~3% V_{tot}) producing large decreases in the band gap. We find a significant drop in band gap at the expected Co_2Si-to-Co_2Si-like phase boundary around 170 $Å^3$, and the $SnCl_2$ data show discontinuities corresponding to the expected phase boundaries in agreement with the calculated HSE06 results.

The observed steepening of band gap with unit-cell volume is likely due to the additive effects of compression and changes in interatomic geometry. Under compression, increased electron orbital overlap broadens the valence and conduction bands, reducing band gaps. Interatomic geometry can further increase electronic orbital overlap as pressure-induced changes in crystal structures force neighboring orbitals into proximity of each other. Recent work shows

the tunability of band gaps with cation-anion bond angles, finding that the band gap decreases as the crystal structure becomes more square-like, in which electron orbitals are forced into overlapping configurations [52-54]. This is consistent with our observations on $PbCl_2$ and $SnCl_2$, in which we observe discontinuous down shifts in the band gap across the transformation from cotunnite to the progressively more close packed-like Co_2Si and Co_2Si-like structures (Fig. 2.4).

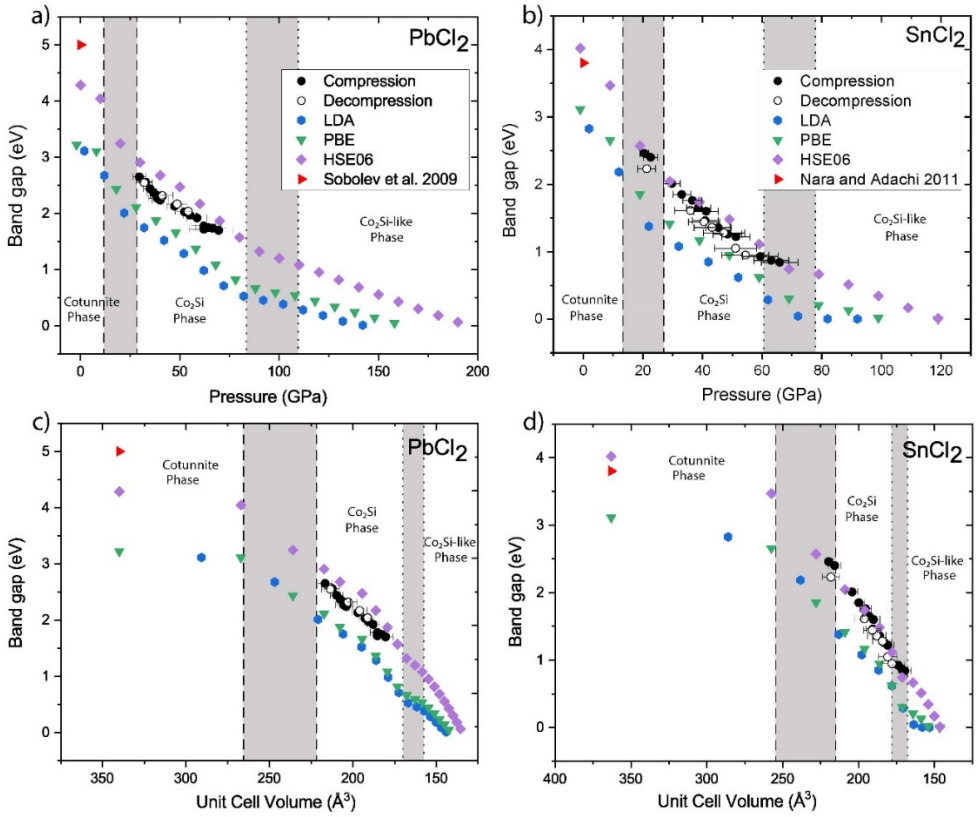

Figure 2.5. Band gap as a function of pressure (*top* panels) and as a function of volume (*bottom* panels) from experiment and theory for $PbCl_2$ (*left*) and $SnCl_2$ (*right*). Zero-pressure band gaps were obtained from Sobolev et al. [50] for $PbCl_2$ and Nara and Adachi [51] for $SnCl_2$. The *gray box* with *dashed lines* shows the pressure range for the transition from the 9-fold coordinated cotunnite to the 10-fold coordinated Co_2Si structure, and the *gray box* with *dotted lines* shows the pressure range for phase transformation from the Co_2Si structure to the 11-fold coordinated Co_2Si-like structure, as labeled in Figs. 2.2 & 2.3. For both $PbCl_2$ and $SnCl_2$, HSE06 fits the data better than either LDA or PBE, albeit with a small overestimation of band gap. (*top*) Extrapolation of our experimental data yields band gap closing pressures of 206 ±24 GPa for $PbCl_2$ and 97 ±6 GPa for $SnCl_2$, in reasonable agreement with theory (200 GPa and 120 GPa respectively). (*bottom*) Volumes for the experimental points are calculated using the equations-of-state model from our compression data. Around 230 $Å^3$ the slope steepens, corresponding to the emergence of the Co_2Si phase and the increase in coordination number in the crystal structure. Extrapolation of our experimental data to band-gap closure yields a closure volume of 131 ±21 $Å^3$ for $PbCl_2$ and 150 ±5 $Å^3$ in $SnCl_2$, in excellent agreement with theory (135 $Å^3$ and 146 $Å^3$ respectively).

Phrased another way, the increased shift in band gap with respect to volume at high compressions has a straightforward physical explanation: the approach to close packing of these materials as they progress through the two phase transitions, coupled with the concomitant increases in both cation and anion coordination, enhances the overlap between the cation conduction (mostly Pb 6*p* and Sn 5*p*) and anion valence (mostly Cl 3*p*) bonding states (see Appendix E). For larger volumes (lower pressures) within the cotunnite structure, the inefficient packing of the anion framework within this quasi-polymeric structure leads to a larger band gap; as the packing becomes more efficient, the rate of band gap decrease is notably enhanced.

CONCLUSIONS

Static compression experiments to over 70 GPa and theoretical simulations to 200 GPa for $PbCl_2$ and 120 GPa for $SnCl_2$ show evidence of a continuous displacive transition from the 9-fold coordinated cotunnite structure to the 10-fold coordinated Co_2Si structure between 17 and 35 GPa in both $PbCl_2$ and $SnCl_2$. Upon further compression, density functionals predict the transition to an 11-fold coordinated Co_2Si-like phase between 75 and 110 GPa in $PbCl_2$ and 60 and 80 GPa in $SnCl_2$, remaining the stable phase through the pressure range of our calculations.

Using equations of state validated by experiments, we calculate band-gap closure using the LDA, PBE, and HSE06 functionals. The hybrid functional HSE06 agrees best with our experimental data, confirming the reliability of HSE06 for calculating the electronic band structure of AX_2 compounds.

Our work shows the relationship between changing interatomic geometry and the closing of the band gap under high pressure, with applications for other AX_2 compounds in both fluid and solid states, which have been demonstrated to transition from low to high coordination number upon compression [6, 7, 9-21]. In particular, our results illustrate that the general pattern of phase transitions in AX_2 compounds from structures that can be viewed as polymeric to those characterized by close-packed anion packing recurs as cation coordination numbers increase under compression. In the particular case of cotunnite relative to the post-cotunnite phases, a distorted but highly coordinated cation environment and complex prismatic anion coordination forms a structure that can be viewed as composed of interlinked polymeric chains, which under compression converges on a phase that approaches close-packing. Our band gap measurements and calculations confirm that such a close-packed anion framework, coupled with high cation coordination numbers, is associated with the metallization of AX_2 oxides [16]. These results are of special interest for SiO_2, a major component of rocky planets that is predicted to exist in the cotunnite phase at pressures corresponding to super-Earth interiors [14]. Previous work investigating the band structure of SiO_2 at these conditions predicts metallization in the I4/mmm phase near 1.4 TPa, though these calculations were preformed using traditional density functionals, motivating the use of hybrid functionals like HSE06 to better constrain the high-pressure band structures [16]. Prediction of metallic SiO_2 could inform us of its potential to influence the dynamics and chemical partitioning in the deep cores of giant planets.

Appendix A: Comparison of experimental and Rietveld-generated XRD Patterns

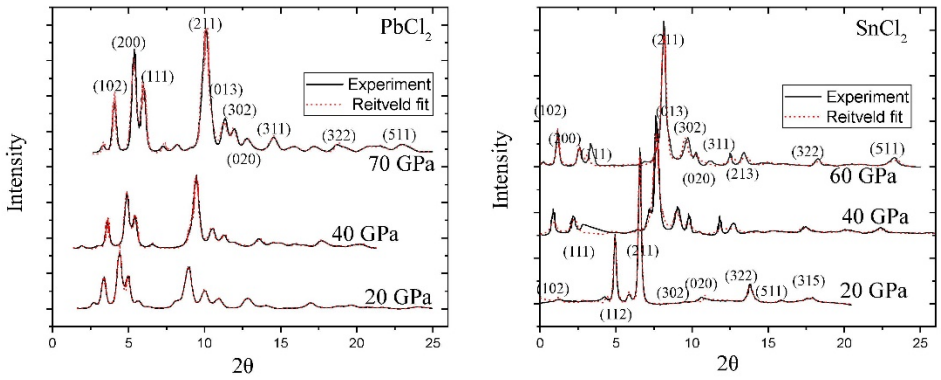

FIG. 2.6: Evolution of observed diffraction pattern as a function of pressure for $PbCl_2$ (top) and $SnCl_2$ (bottom). Patterns generated with Rietveld refinements (dashed lines) agree with experimental results at all pressures. The shoulder in the experimental data seen in the $SnCl_2$ data near the (111) peak is likely an artifact due to background subtraction.

Appendix B: Fits for Equations of State

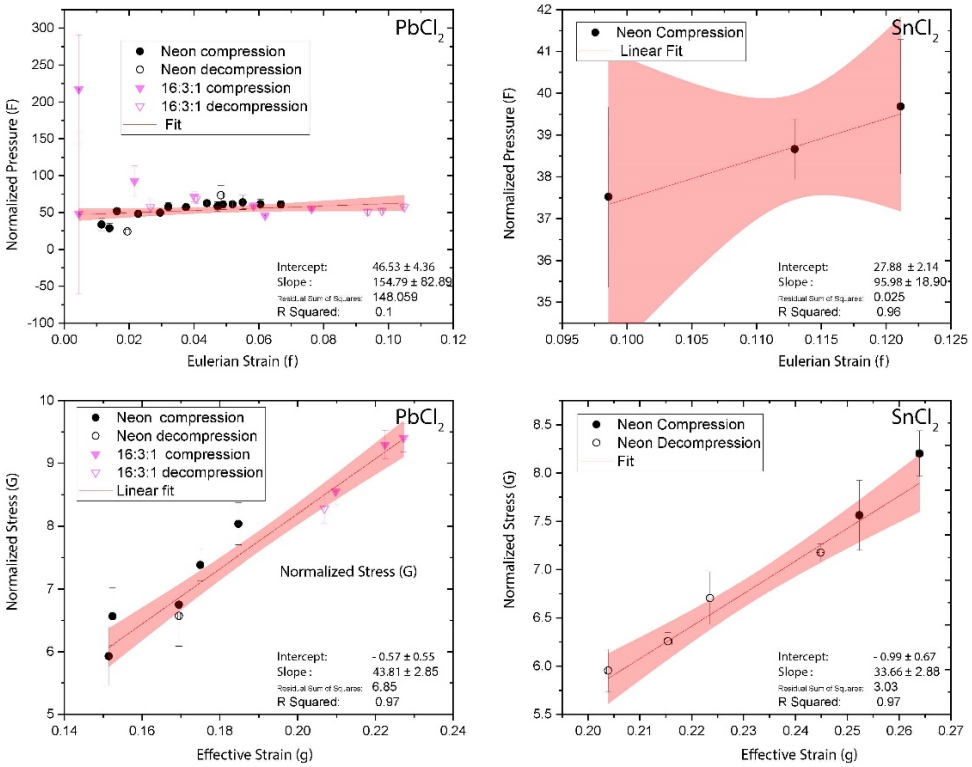

Fig. 2.7. Eulerian strain vs. normalized strain (F vs. f) and effective strain vs. normalized strain (G vs. g) are shown for $PbCl_2$ and $SnCl_2$. F vs. f plots were used to determine the equations of state for the low-pressure phases, while G vs. g was used for high-pressure phases [44]. Data from the phase transition zone fit neither equation of state and were thus omitted. A weighted least-squares fit was applied to each data set (red lines) and 95% confidence intervals are shown (red shading).

Appendix C: Using ratios of the lattice parameters to determine phase changes:

The transformation between the cotunnite and Co_2Si structures is characterized by a shift in the ratios of lattice parameters and a change in coordination from 9- to 10-fold. Jeitschko [42] and Leger et al. [10] show that the a/c and (a+c)/b ratios distinguish between phases with orthorhombic (*Pnma*) symmetry. These ratios were later updated by Stan et al. [15], who show that for the cotunnite structure a/c = 0.8-0.9 and $(a+c)/b$ = 3.3-4.0, and for Co_2Si a/c = 0.7-0.78 and $(a+c)/b$ = 2.90-3.56. When our data are plotted using these ratios, we see a clear distinction between the cotunnite and Co_2Si phases (Fig. 8). Points that fall between the two phases are between 17 and 27 GPa for $PbCl_2$ and 17 and 33 GPa for $SnCl_2$. LDA and PBE calculations follow experimental data closely over the pressure range of our experiments. Here, the shift to the distorted Co_2Si-like phase is seen as a strong inflection point toward higher $(a+c)/b$ values near $(a+c)/b$ = 3.2.

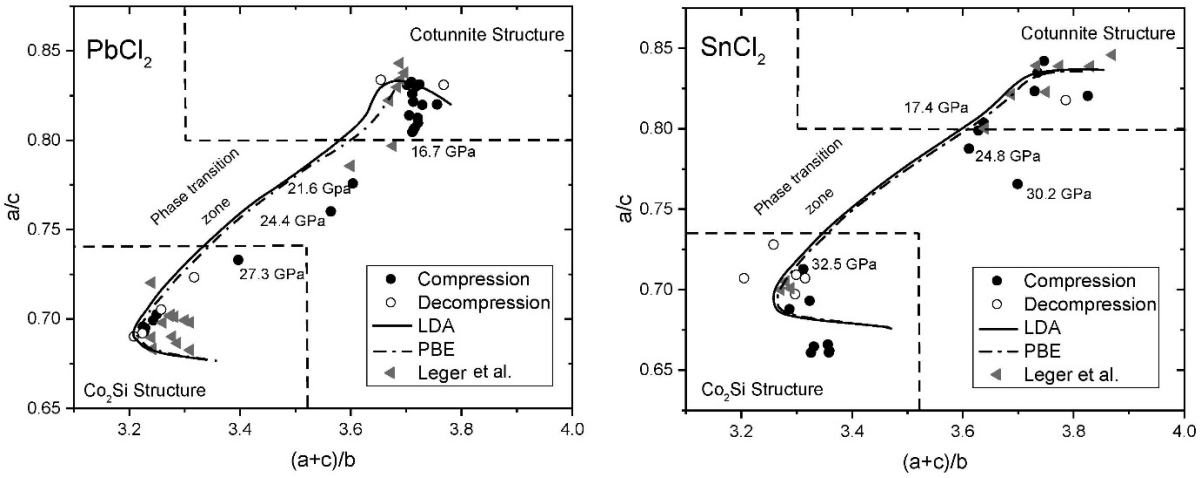

Fig. 2.8 . Lattice parameter ratios of $PbCl_2$ (left) and $SnCl_2$ (right). Borders that define the phases follow Stan et al. [15]. Circles are data from this study, with solid circles indicating data taken on compression and empty circles those taken on decompression. Data from Leger et al. [12] are plotted as gray triangles. Calculated lattice ratios are shown as the solid (LDA) and dash-dot (PBE) curves.

Appendix D: Absoption edge spectroscopy with pressure

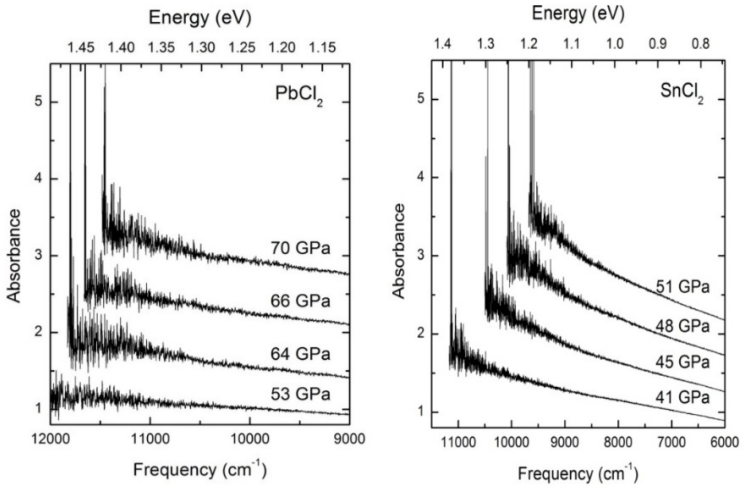

FIG. 2.9. Representative high-pressure spectra of the absorption edge of $PbCl_2$ (a) and $SnCl_2$ (b). No exciton peaks are resolved within these experiments. These spectra show that the energy of the band gap *decreases* as pressure *increases*. Spectra are stacked for clarity.

Appendix E: Density of States Calculations

The partial density of states for $PbCl_2$ & $SnCl_2$ calculated using the HSE06 exchange-correlation functional shows that the valence band has primarily Cl 3*p* and Pb, Sn 6*s* character. The unoccupied conduction band has mainly Pb, Sn 6*p* and diminished Cl 3*p* character. All bands broaden with increasing pressure, as band gap reduces from about 4 eV at ambient pressure in each $PbCl_2$ and $SnCl_2$ to closure.

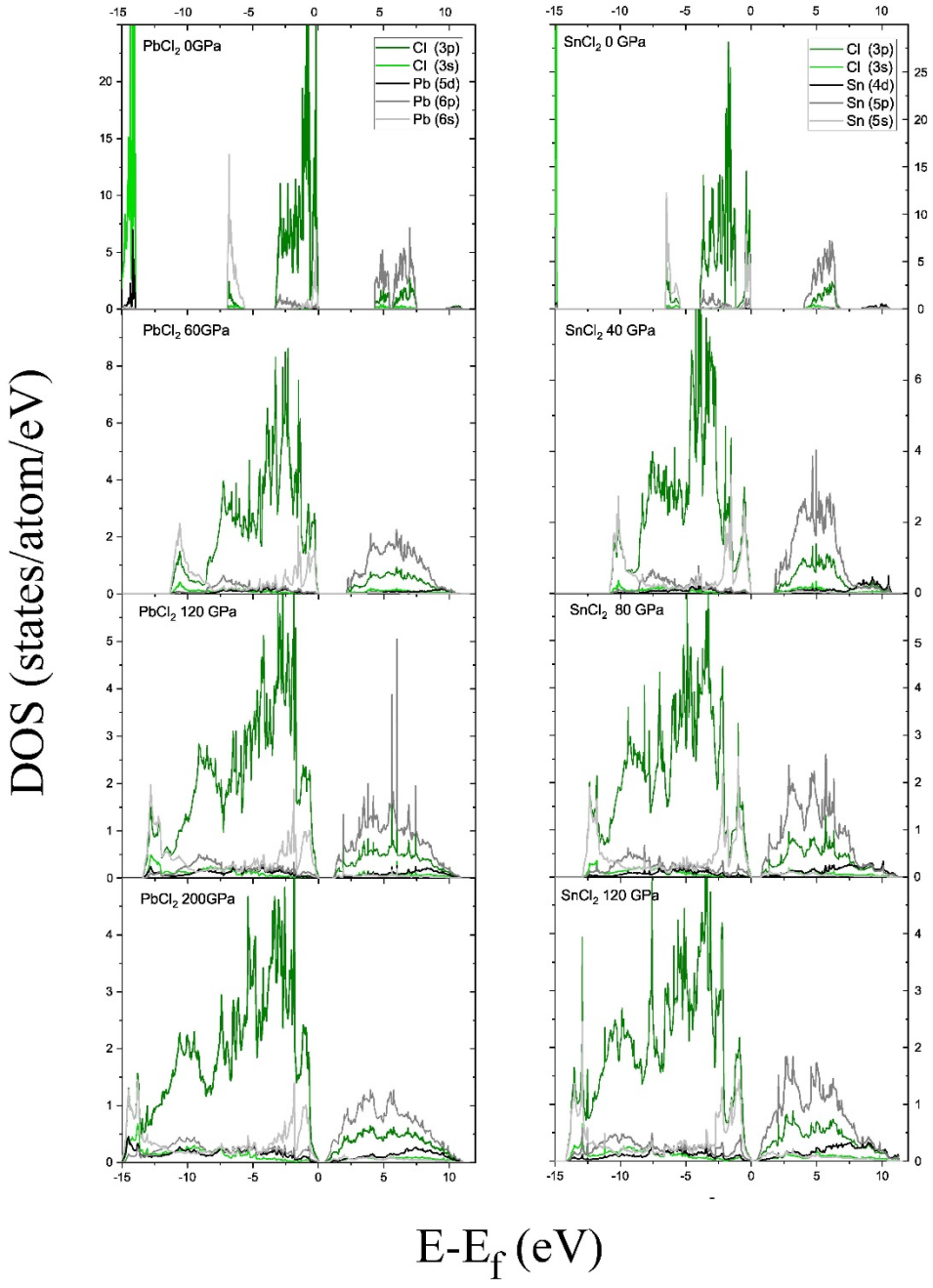

Fig 2.10: Calculated density of states (DOS) for $PbCl_2$ at 0, 60, 120, and 200 GPa (left) and $SnCl_2$ at 0, 40, 80, and 120 GPa (right) using HSE06 density functional. Ambient pressure DOS (*top panels*) show a clear distinction between *s* & *p* orbitals in both Pb, Sn and Cl, with an energy gap of around 4 eV. We observe a broadening of all states to higher pressure (*downward panels*).

Appendix F: Experimental Data

Table 2.2: Experimental Data: Pressures, Unit Cell Volume, and Lattice parameters.

	Pressure (GPa)		Volume (Å^3)		a (Å)		b (Å)		c (Å)	
$PbCl_2$	1.6	0.2	299.20	0.15	7.556	0.001	4.412	0.001	8.973	0.005
	8.3	2.6	292.50	0.10	7.459	0.002	7.000	0.004	8.935	0.004
	10.8	2.3	286.85	0.15	7.358	0.002	4.369	0.005	8.937	0.006
	14.6	2.6	277.10	0.13	7.319	0.002	4.244	0.004	8.920	0.005
	17.4	3.0	242.80	0.10	6.813	0.011	4.203	0.006	8.478	0.002
	21.8	2.4	234.31	0.10	6.707	0.001	4.162	0.001	8.394	0.001
	24.8	3.0	229.70	0.15	6.602	0.001	4.150	0.001	8.383	0.002
	30.3	4.0	215.33	0.10	6.419	0.001	4.002	0.002	8.383	0.003
	32.6	4.6	201.92	0.10	5.709	0.002	4.262	0.001	8.300	0.000
	36.1	0.3	203.70	0.10	5.770	0.002	4.241	0.001	8.325	0.003
	41.0	2.6	195.60	0.10	5.770	0.004	4.187	0.002	8.096	0.004
	45.1	2.0	181.70	0.13	5.455	0.004	4.066	0.004	8.191	0.004
	51.7	1.6	176.99	0.04	5.392	0.002	4.030	0.003	8.145	0.002
	57.0	1.4	174.82	0.05	5.365	0.002	4.015	0.004	8.117	0.003
	63.0	3.0	172.32	0.06	5.321	0.002	4.021	0.004	8.053	0.003
	71.0	2.0	168.40	0.20	5.300	0.006	3.984	0.007	7.973	0.007
	67.1	1.8	176.70	0.10	5.556	0.005	4.047	0.003	7.859	0.003
	58.3	0.7	174.92	0.10	5.486	0.002	4.051	0.000	7.870	0.000
	50.7	2.1	182.70	0.02	5.618	0.001	4.104	0.001	7.923	0.002
	46.0	0.6	185.82	0.30	5.770	0.005	4.203	0.007	7.926	0.005
	42.0	1.6	190.40	0.11	5.632	0.005	4.243	0.004	7.966	0.004
$SnCl_2$	1.6	0.2	299.20	0.15	7.556	0.001	4.412	0.001	8.973	0.005
	8.3	2.6	292.50	0.10	7.459	0.002	7.000	0.004	8.935	0.004
	10.8	2.3	286.85	0.15	7.358	0.002	4.369	0.005	8.937	0.006
	14.6	2.6	277.10	0.13	7.319	0.002	4.244	0.004	8.920	0.005
	17.4	3.0	242.80	0.10	6.813	0.011	4.203	0.006	8.478	0.002
	21.8	2.4	234.31	0.10	6.707	0.001	4.162	0.001	8.394	0.001
	24.8	3.0	229.70	0.15	6.602	0.001	4.150	0.001	8.383	0.002
	30.3	4.0	215.33	0.10	6.419	0.001	4.002	0.002	8.383	0.003
	32.6	2.6	201.92	0.10	5.709	0.002	4.262	0.001	8.300	0.000
	36.1	0.3	203.70	0.10	5.770	0.002	4.241	0.001	8.325	0.003
	41.0	2.6	195.60	0.10	5.770	0.004	4.187	0.002	8.096	0.004
	45.1	2.0	181.70	0.13	5.455	0.004	4.066	0.004	8.191	0.004
	51.7	1.6	176.99	0.04	5.392	0.002	4.030	0.003	8.145	0.002
	57.0	1.4	174.82	0.05	5.365	0.002	4.015	0.004	8.117	0.003
	63.0	3.0	172.32	0.06	5.321	0.002	4.021	0.004	8.053	0.003
	71.0	2.0	168.40	0.20	5.300	0.006	3.984	0.007	7.973	0.007
	67.1	1.8	176.70	0.10	5.556	0.005	4.047	0.003	7.859	0.003
	58.3	0.7	174.92	0.10	5.486	0.002	4.051	0.000	7.870	0.000
	50.7	2.1	182.70	0.02	5.618	0.001	4.104	0.001	7.923	0.002
	46.0	0.6	185.82	0.30	5.770	0.005	4.203	0.007	7.926	0.005
	42.0	1.6	190.40	0.11	5.632	0.005	4.243	0.004	7.966	0.004
	0.0	0.0	318.03	0.05	7.623	0.002	4.476	0.003	9.322	0.006

Table 2.2: Experimental Data: Measured pressures, volumes and lattice parameters for SnCl2 and PbCl2 on compression and decompression. The determined value for each measured parameter is shown in the first column, and the confidence band is shown in the second column. Volumes and lattice parameters were obtained though Rietveld refinement of our XRD data, and pressures were determined using the standard ruby fluorescence technique [24].

References

[1] L. Stixrude and R. Jeanloz, Proceedings of the National Academy of Sciences of the United States of America 105, 11071 (2008).
[2] P. M. Celliers, P. Loubeyre, J. H. Eggert, S. Brygoo, R. S. McWilliams, D. G. Hicks, T. R. Boehly, R. Jeanloz and G.W. Collins, Physical Review Letters 104, 184503 (2010).
[3] L. Pauling, The Nature of the Chemical Bond 3rd Edition, (Cornell University Press), (Ithaca New York), (1960)
[4] M. Millot, N. Dubrovinskaia, A. Cernok, S. Blaha, L. Dubrovinsky, D.G. Braun, P.M. Celliers, G.W. Collins, J.H. Eggert, R. Jeanloz, Science 347, 418 (2015).
[5] H. Shu et al., Physics of Plasmas 27, 4, 030701 (2020).
[6] B. Kalkan, B. Godwal, S. V. Raju, and R. Jeanloz, Scientific Reports 8, 10, 6844 (2018).
[7] A. Denoeud, S. Mazevet, F. Guyot, F. Dorchies, J. Gaudin, A. Ravasio, E. Brambrink, and A. Benuzzi-Mounaix, Physical Review E 94, 5, 031201 (2016).
[8] E. M. Stolper and T. J. Ahrens, Geophysical Research Letters 14, 1231 (1987).
[9] J. M. Leger, J. Haines, and A. Atouf, Journal of Applied Crystallography 28, 416 (1995).
[10] J. M. Leger, J. Haines, A. Atouf, O. Schulte, and S. Hull, Physical Review B 52, 13247 (1995).
[11] J. M. Leger, J. Haines, and A. Atouf, Physical Review B 51, 3902 (1995).
[12] J. M. Leger, J. Haines, and A. Atouf, Journal of Physics and Chemistry of Solids 57, 7 (1996).
[13] J. Haines, J. M. Leger, and O. Schulte, Journal of Physics-Condensed Matter 8, 1631 (1996).
[14] A. R. Oganov, M. J. Gillan, and G. D. Price, Physical Review B 71, 8, 064104 (2005).
[15] C. V. Stan, R. Dutta, C. E. White, V. Prakapenka, and T. S. Duffy, Physical Review B 94, 12, 024104 (2016).
[16] M. J. Lyle, C. J. Pickard, and R. J. Needs, Proceedings of the National Academy of Sciences of the United States of America 112, 6898 (2015).
[17] O. Ohtaka, D. Andrault, P. Bouvier, E. Schultz, and M. Mezouar, Journal of Applied Crystallography 38, 727 (2005).
[18] S. R. Shieh, A. Kubo, T. S. Duffy, V. B. Prakapenka, and G. Shen, Physical Review B 73, 7, 014105 (2006).
[19] S. J. Duclos, Y. K. Vohra, A. L. Ruoff, A. Jayaraman, and G. P. Espinosa, Physical Review B 38, 7755 (1988).
[20] H. X. Song, L. Liu, H. Y. Geng, and Q. Wu, Physical Review B 87, 9, 184103 (2013).
[21] S. Duwal, C.A. McCoy, P.F. Weck, P. Kalita, H. L. Hanshaw, K. Cochrane, T. Ao, S. Root, Physical Review B 102 024105 (2020)
[22] P. J. Hasnip, K. Refson, M. I. J. Probert, J. R. Yates, S. J. Clark, and C. J. Pickard, Philosophical Transactions of the Royal Society a-Mathematical Physical and Engineering Sciences 372, 26, 20130270 (2014).
[23] Perdew, J.P. and Levy, M., Physical Review Letters, 51(20), 1884-1887, 1983
[24] A. Dewaele, M. Torrent, P. Loubeyre, and M. Mezouar, Physical Review B 78, 13, 104102 (2008).
[25] Q. Williams and R. Jeanloz, Physical Review Letters 56, 163 (1986).
[26] A. P. Hammersley, S. O. Svensson, M. Hanfland, A. N. Fitch, and D. Hausermann, High Pressure Research 14, 235 (1996).
[27] C. Prescher and V. B. Prakapenka, High Pressure Research 35, 223 (2015).
[28] A.C., Larson and R.B., Von Dreele , Alamos National Laboratory Report LAUR 86-748. (2004).
[29] G. Kresse and J. Furthmuller, Computational Materials Science 6, 15 (1996).
[30] G. Kresse and J. Furthmuller, Physical Review B 54, 11169 (1996).
[31] P. E. Blochl, Physical Review B 50, 17953 (1994).
[32] G. Kresse and D. Joubert, Physical Review B 59, 1758 (1999).
[33] J. P. Perdew and A. Zunger, Physical Review B 23, 5048 (1981).
[34] J. P. Perdew, K. Burke, and M. Ernzerhof, Physical Review Letters 77, 3865 (1996).
[35] H. Xiao, J. Tahir-Kheli, and W. A. Goddard, Journal of Physical Chemistry Letters 2, 212 (2011).
[36] A. V. Krukau, O. A. Vydrov, A. F. Izmaylov, and G. E. Scuseria, Journal of Chemical Physics 125, 5, 224106 (2006).
[37] A. J. Garza and G. E. Scuseria, Journal of Physical Chemistry Letters 7, 4165 (2016).
[38] H. J. Monkhorst and J. D. Pack, Physical Review B 13, 5188 (1976)
[39] A. R. Oganov, J. P. Brodholt, and G. D. Price, Earth and Planetary Science Letters 184, 555 (2001).
[40] B. K. Godwal, S. Stackhouse, J. Yan, S. Speziale, B. Militzer, and R. Jeanloz, Physical Review B 87, 5, 100101 (2013).
[41] B.G. Hyde, M. O'Keeffe, W.M. Lyttle, and N.E. Brese, Acta Chemica Scandinavica, 46, 216-223 (1992).
[42] W. Jeitschko, Acta Crystallographica Section B-Structural Crystallography and Crystal Chemistry B 24, 930 (1968).
[43] I. Abrahams, and D.Z. Demetriou, Journal of Solid State Chemistry, 149, 28-32 (2000).
[44] R. Jeanloz, Journal of Geophysical Research-Solid Earth and Planets 94, 5873 (1989). [
[45] K. Momma and F. Izumi, Journal of Applied Crystallography, 44, 1272 (2011).
[46] S. Froyen and M.L. Cohen, Journal of Physics-C, Solid State Physics, 19, 2623 (1986).
[47] P. Cervantes, Q. Williams, M. Cote, M. Rohlfing, M.L.Cohen and S.C. Louie, Physical Review B, 58, 9793 (1998).
[48] N.E. Christensen, A. Svane, and E. Peltzer y Blanca, Physical Review B, 72, 014109 (2005).
[49] J.-M. Raulot, G. Baldinozzi, R. Seshadri, and P. Cortona, Solid State Sciences, 4, 467 (2002).
[50] V. V. Sobolev, A. I. Kalugin, and I. V. Vostrikov, Journal of Surface Investigation-X-Ray Synchrotron and Neutron Techniques 3, 48 (2009)
[51] J. Nara and S. Adachi, Journal of Applied Physics 109, 7, 083539 (2011).
[52] L. Zhang, K. Wang, and B. Zou, The Journal of Physical Chemistry Letters, 11, 4693 (2020)
[53] R. K. Hona, and F, Ramezanipour, Journal of Chemical Sciences, 131, 12039, (2019).
[54] M.R. Filip, G. E. Eperon, H. J. Snaith, and F Guistino, Nature Communications, 5, 5757 (2014).

Chapter 3:

High-Pressure Nano-Seismology: Use of Micro-Ring Resonators for Characterizing Acoustic Emissions

Micro-ring resonator (MRR) ultrasound detectors provide orders of magnitude greater sensitivity and frequency range (to < 10 Pa, from DC to 100s of MHz) than previously achieved in recording acoustic emissions from materials at high pressures. We characterize acoustic emissions from crystal-structural phase transitions in Si to pressures of 50 GPa, well beyond the brittle-ductile transition at room temperature, and find that the number of events increases nearly tenfold for each decade reduction in the duration of recorded events. The shortest-duration events arrive in clusters, suggestive of a self-propagating, transformation-catalyzed process.

Acoustic emissions present a fundamental conundrum in the deformation behavior of materials at pressures exceeding 1-3 GPa, because yielding is by ductile flow rather than brittle fracture at these pressures.[1] This is due to the normal forces across incipient shear planes being sufficiently large to prevent fracture in the material. Still, emissions have been documented in connection with phase transformations at pressures well above the brittle-ductile transition,[2-6] using detectors sensitive to frequencies of 2-20 MHz. Given that the time for an acoustic wave to traverse the samples in these studies is on the order of 10^{-7} seconds,[2] and is comparable to the sampling rate, past work has been limited in its ability to resolve fine detail in the acoustic emissions of materials at high pressures.

Here we describe an opto-electronic method for characterizing acoustic emissions from samples at high pressure, the objective being to increase sensitivity and frequency range relative to past capabilities.[7,8] Briefly, the micro-ring resonator uses tunneling of light (evanescent waves) between a through-going optical bus waveguide and whispering gallery modes (WGM) in a neighboring ring waveguide (Fig. 3.1). The underlying optical resonance provides high sensitivity to transient-pressure induced modulation of the resonance mode, down to less than 10 Pa as compared with 1-55 kPa typical of commercial piezoelectric sensors.[9] Sensitivity is also enhanced by using a soft (compliant) polymeric material, in our case polystyrene.

Because light modulation carries the signal, the sensor is in principle responsive to frequencies into the THz range. As described below, however, our current system is effective only up to frequencies of ~ 250 MHz: still 1-2 orders of magnitude higher than for previous high-pressure measurements.[3,5,6] For a shear-wave velocity of 5 km/s, this implies sensitivity to acoustic wavelengths down to ~20 μm, comparable to our sample dimensions and approaching the size of grains, if not the stress field at shear- and tensile-fracture tips for Si at ambient conditions (the process zone of ductile deformation at the fracture tip is yet smaller, ~2-5 nm). [10-14]

Silicon powder (grain size ~10 μm) was compressed in Merrill-Basset type diamond-anvil cells without any pressure medium, as our intent was to generate shear stresses under high pressure.

The diamonds had culet diameters of 350 μm, paired with a 250 μm-thick spring-steel gasket pre-compressed to 70-90 μm thickness and containing a 150 μm-diameter hole as the sample chamber. A film of ruby powder ~5 μm thick (~1 μm grain size) was added to the culet of one of the diamonds for pressure calibration, using ruby fluorescence.[15]

As described by Li and Dong et al.,[7] the micro-ring resonator (MRR) ultrasound detector is placed on a 2 mm × 2 mm fused silica coverslip. The polystyrene optical waveguide has a square-shaped cross-section, 800 nm across, and both the input and output ends of this bus waveguide are precisely cleaved for fiber coupling. To excite optical resonance in the MRR, a narrow-band continuous-wave (CW) tunable laser (New Focus, TLB-6712, wavelength 765 nm to 781 nm) is coupled into the bus waveguide after passing through a fiber polarization controller. On the other end of the bus waveguide, a multimode fiber and photodetector (Newport, 2107-FC) are used to measure the transmitted light intensity.

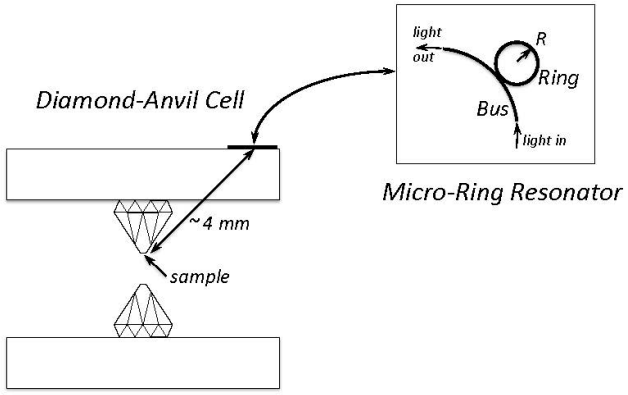

Fig. 3.1. Schematic of micro-ring resonator and diamond-anvil cell used in the present experiments (not to scale). Light transmitted down the bus fiber is evanescently coupled into the ring (radius R ~ 30 μm), such that an acoustic wave temporally modulates the light exiting the bus. The polystyrene fiber optics are placed on a 2 x 2 mm silica glass slide, which is attached to the body of the diamond cell. The location of the sample is between the diamond tips (culets), and for clarity no gasket is shown.

The light inside the bus waveguide is evanescently coupled into the ring waveguide across a low-dielectric gap between the bus and ring. Light circulating inside the ring waveguide leads to a strong optical resonance be characterized by a narrow dip in the transmission spectrum due to destructive interference between light in the two waveguides. Minimum transmission is achieved at the resonance wavelength (λ_r) at critical coupling, when the intrinsic loss of the ring resonator matches the coupling loss. The quality (Q) factor of the MRR is determined from the measured transmission spectrum, $T(\lambda)$, as $\lambda_r/\Delta\lambda = 1.2 \times 10^5$, where $\Delta\lambda$ is the full width at half-maximum of the resonance dip. The MRR operating wavelength is set slightly off-resonance, at the waist of the resonance dip, to achieve an optimal detection sensitivity of $dT/d\lambda = 30.24$ nm^{-1} at 776.25 nm.

Acoustic waves induce changes in both the dimension and refractive index of the polymer ring, collectively altering the optical path length of the ring resonator, thus shifting the resonant frequency. The shift in resonant frequency is measured as a voltage modulation in the transmitted optical signal by a photodetector. We used a low-noise, high-sensitivity avalanche photodiode (APD, Hamamatsu c4777) to record the transmitted light through the bus waveguide. The detected

signals were then amplified by 12 dB (Mini-circuits ZFL500NL+, 500-MHz bandwidth), and digitized by a high-speed digitizer (CobraMax, GaGe; sampling rate:$3x10^9$ samples/s, bandwidth: 1.5 GHz). This sensor provides a broad detection band of over 100 MHz, and a pressure detection limit of 6.8 Pa.

The MRR assembly was mounted on the steel body of the diamond-anvil cell (Fig. 3.1), which was held in a clamp mounted to an air-floating optical table, and elevated above the surface of the table to reduce ambient noise. Samples were compressed at room temperature up to pressures of 50 GPa, and acoustic emissions were monitored during both compression and decompression cycles. The MRR detector was about 4 mm away from the polycrystalline silicon sample, and was set to trigger during and after the pressure changes were being applied. All measurements were made at 19-22˚ C.

A series of control experiments were conducted to pressures exceeding 35 GPa, using both steel and rhenium gaskets. Inside the sample chamber, we loaded i) no pressure medium (in order to record any acoustic emissions from the empty sample chamber closing); ii) a neon pressure medium; or iii) a 4:1 methanol:ethanol pressure medium. We also ran tests on plain metal foils (i.e., gaskets with no sample chamber) to further test the gasket material for acoustic emission. None of these control experiments yielded any acoustic emissions, indicating that the signals we report over this pressure range are caused by deformation of the silicon sample.

We recorded acoustic emissions in silicon to 17 GPa on compression and decompression, well above the brittle-ductile transition, estimated around 1.5 GPa at room temperature,[14] as confirmed by observing the sample to flow in a ductile manner during compression. During the initial compression, acoustic emissions were measured at the Si-I (diamond structure) → Si-II (β-Sn structure) transformation between 11-12 GPa. On further compression, emissions were recorded acoustic signals between 16 and 17 GPa, corresponding to the Si-XI (orthorhombic, *Imma*) → Si-V (simple hexagonal) transition. Signals were also recorded on decompression from the high-pressure Si phases to the metastable Si-III (bcc) phase around 11 GPa (see Table 3.1).[2,16-19] Cycling the sample by decompression and recompression into low- and high-pressure phases consistently yielded acoustic emissions at these conditions. In contrast, we recorded no acoustic emissions while crossing the Si-II → XI, V→VI, and VI→VII phase transitions at ~15, ~34 and ~40 GPa, respectively, either during compression or decompression. Evidently, not all phase transitions produce acoustic emissions, at least over the frequency range and within the sensitivity of our detection system (this point is also relevant to the lack of acoustic emissions from any of our present gasket materials).

	Phase Transition	Pressure Range (GPa)	Maximum Emission Duration (s)
	Si-I→ Si-II	11-12	10^{-7}
Compression			
	Si-II→ Si-XI	13-15	No Emission
	Si-XI→ Si-V	16-17	10^{-3}
Decompression	Si-V→ Si-III	9-11	10^{-4}
Recompression	Si-III→ Si-V	13-17	10^{-5}

Table 3.1. Phase transitions and corresponding pressure ranges during which we observe acoustic emission in Si at room temperature. All transitions associated with acoustic emissions yielded acoustic events on the order of 10^{-7}s, though the maximum duration appears to vary between different phase transitions. The maximum duration of recorded acoustic events are shown.

The duration of individual acoustic events from our samples ranges from 10^{-7}s to 10^{-3} s, roughly following a power law with the number of emissions, decreasing by nearly one order of magnitude for each decade increase in duration (exponent ~0.8-1.0) (Fig. 3.2, *left panel*). For a given rupture, the event duration is proportional to the seismic moment and magnitude, allowing us to compare this result with moment-magnitude distributions observed in seismology (e.g., Gutenberg-Richter law). Our results closely follow observations made in past laboratory and field observations of rupturing, including of acoustic emissions from high-pressure multi-anvil experiments.

Samples that produce only short emissions on compression often yield additional signals upon further compression, but this was not the case for samples emitting signals longer than ~10^{-5} s. Emissions with durations on the order of 1 ms were audible at a distance of ~1 m, and the resulting deformation of the sample was visible under the microscope, with displacements exceeding 1-10 μm. Acoustic emissions shorter than 10^{-3} s were not audible, and showed no visible sample deformation.

Short (~200 ns) emissions are observed for all of the acoustically active phase transitions, both on their own and as part of longer events. Comparison of these short emissions between sample runs shows a consistent structure of three pulses, each about 60 ns long (Fig. 3.2, *bottom of middle panel*), and with peak frequencies of 120-140 MHz. Acoustic events longer than 10^{-7} s displayed peak frequencies identical to those of the shortest emissions, as well as at lower frequencies as would be expected. These longer events consist of a high density of short emissions, as also indicated by the >100 MHz peaks in the power spectra (Fig. 3.2, *middle of right panel*).

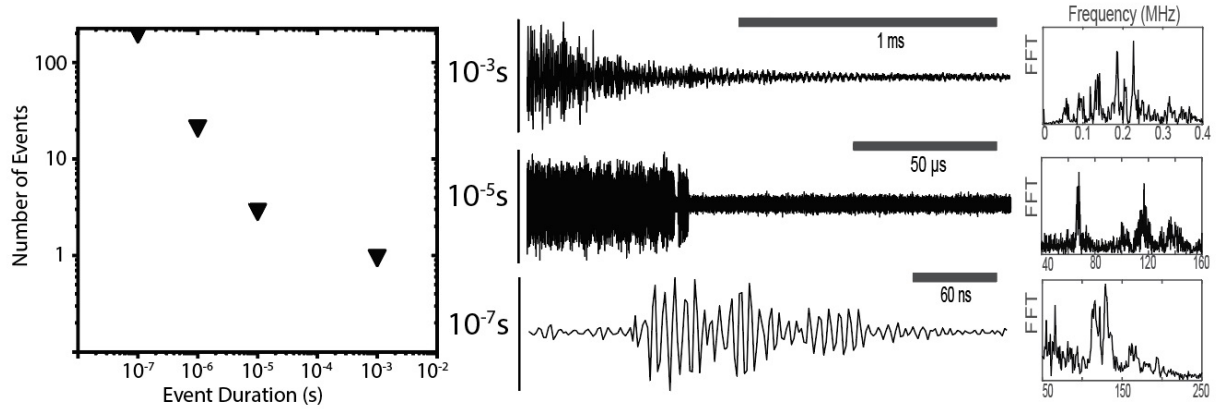

Fig. 3.2. Acoustic signals collected from Si between 14 and 17 GPa, showing that the number of events decreases with increased event duration (*left*). Signals with durations of 10^{-5} seconds and 10^{-7} seconds (*middle*) have strong peaks around 120 MHz in their power spectra (*right*), corresponding to wavelengths comparable to or smaller than the thickness of our sample chamber. Signals approaching millisecond duration exhibit a significantly different power spectrum, with no signal recorded above 0.5 MHz, suggesting either a change in failure mechanism or that the amplitude of the low-frequency emission obscures higher-frequency signals.

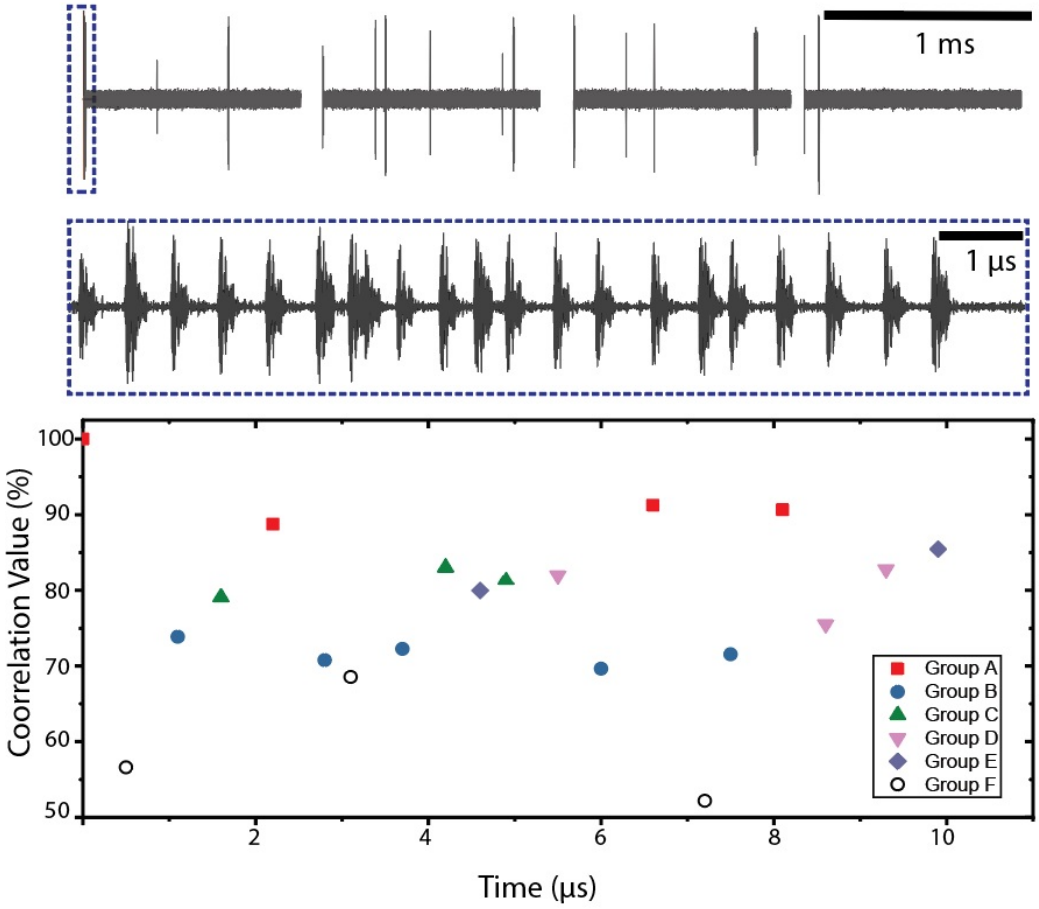

Fig. 3.3. A ~5 ms record is shown (*top*), displaying acoustic-emission bursts at apparently random intervals. Each burst at the millisecond timescale is found to consist of several roughly periodic emissions (*middle*). Cross correlation (*bottom*) shows 50-90% correspondence between the first signal ($0 < t < 0.4$ µs) and subsequent emissions (*open symbols*, plotted directly below each given emission). Groups, identified as signals having similar correlation values relative to the primary emission, are also found to produce significantly higher (85-95%) correlations when compared with one another (*filled, color symbols*: none for Group F), suggesting similarities in source mechanisms for signals in a group.

When short-duration (~200 ns) signals are not part of a longer signal, there is a tendency for the emissions to cluster into groups of 5-20 events. These clusters do not show the high correlations and decaying amplitudes one would expect from successive echoes, so are interpreted as individual nano-seismic events (Fig. 3.3). Short-duration emissions show cross-correlations ranging between 70 and 90%. Also, emissions with similar correlation value to a given signal (e.g., the initial burst) show high (85-95%) mutual correlations (closed symbols in Fig. 3.3), suggesting that the emissions within that group are related. These mutually correlated emissions may have sources that are similar in orientation or other characteristics. Note that a 100 ns signal implies a rupture propagating across the full diameter of our sample (150 µm) for a rupture velocity less than 1/3 the shear-wave velocity (V_S is 5 km/s or 5 µm/ns at zero pressure).

The temporal spacing between acoustic clusters appears random (Fig 3.3, *top panel*). When subjected to a test of randomness, the intervals are found to follow a Poisson distribution with an average of 0.24 events per µs, implying that the clusters are independent of each other. However, the temporal spacing is more regular within a given cluster (Fig 3.3, *middle panel*), suggesting a catalytic process in which one acoustic emission triggers subsequent events in the cluster.

References

1. M. S. Paterson and T.-F. Wong, *Experimental Rock Deformation – The Brittle Field*, 2nd Ed.(Springer, New York, 2005) pp 211-237.
2. C. Meade and R. Jeanloz, Nature 339 (6226), 616 (1989).
3. C. Meade and R. Jeanloz, Science 252 (5002), 68 (1991).
4. A. A. de Ronde and D. P. Dobson, High Pressure Research 28 (1), 9 (2008).
5. A. Schubnel, F. Brunet, N. Hilairet, J. Gasc, Y. B. Wang and H. W. Green, Science 341 (6152), 1377 (2013).
6. H. M. Wei and S. Krishnaswamy, Optics Letters 42 (13), 2655 (2017).
7. H. Li, B. Q. Dong, Z. Zhang, H. F. Zhang and C. Sun, Scientific Reports 4, 8 (2014).
8. H. Wei, A. K. Amrithanath and S. Krishnaswarmy, Health Monitoring of Structural and Biological Systems XII, doi:10.1117/12.2296273 (2018).
9. B. Q. Dong, C. Sun and H. F. Zhang, Ieee Transactions on Biomedical Engineering 64 (1), 4 (2017).
10. A. G. Haerle, W. R. Cannon and M. Denda, Journal of the American Ceramic Society 74 (11), 2897 (1991).
11. I. Chasiotis, S. W. Cho and K. Jonnalagadda, Journal of Applied Mechanics-Transactions of the Asme 73 (5), 714 (2006).
12. R. F. Cook, Journal of Materials Science 41 (3), 841 (2006).
13. B. N. Jaya, J. M. Wheeler, J. Wehrs, J. P. Best, R. Soler, J. Michler, C. Kirchlechner and G. Dehm, Nano Letters 16 (12), 7597 (2016).
14. H. J. Frost and M. F. Ashby, *Deformation Mechanism Maps*, (Pergamon, Oxford, UK, 1982) pp.71-74
15. H. K. Mao, J. Xu and P. M. Bell, Journal of Geophysical Research-Solid Earth and Planets 91 (B5), 4673 (1986).
16. J. Z. Hu and I. L. Spain, Solid State Communications 51 (5), 263 (1984).
17. H. Olijnyk, S. K. Sikka and W. B. Holzapfel, Physics Letters A 103 (3), 137 (1984).
18. M. I. McMahon, R. J. Nelmes, N. G. Wright and D. R. Allan, Physical Review B 50, 739 (1994).
19. A. Kubo, Y. Wang, C. Runge, T. Uchida, B Kiefer, N Nishiyama, T. Duffy, Journal of Physics and Chemistry of Solids 69 (9), 2255 (2008)

Chapter 4:

Nano-Seismic Shear Sources from Serpentine at Lower mantle Pressures

Abstract

We determine displacements for acoustic emissions recorded during solid-state transformation of serpentine at 6 to 26 GPa, pressures extending well into those of Earth's lower mantle. All experimentally observed nano-seismic events exhibit significant shear components, similar to findings from naturally occurring deep-focus earthquakes. Our laboratory observations suggest that nano-seismic events are the results of a repeating failure process.

Main Text:

The failure mechanism for deep-focus earthquakes is poorly understood, with events occurring to 700 km depth, at pressure-temperature conditions well beyond expected ~60 km limit of elastic failure (*1-3*). Laboratory observations of acoustic emissions during crystal-structural transitions of mantle minerals provide an attractive hypothesis for the failure mechanism responsible for deep earthquakes, in which pressure-induced volume collapse associated with mineral transformations causes local stress instabilities that lead to failure and release of acoustic energy (*4-8*). However, deep earthquakes are invariably double-couple sources, with no evidence of volume collapse (*3*).

Here we characterize the acoustic emissions from chrysotile serpentine between 6 and 26 GPa on compression and decompression, showing that shear – not volumetric – displacements are generated by high-pressure transformation. Serpentine is representative of the minerals that sink into the mantle at subduction zones, the regions where deep-focus earthquakes are observed. We use a diamond cell instrumented with 4 displacement sensors sampling at 0.1-40 MHz; three of the sensors are in the plane of the sample, perpendicular to the loading axis, and a fourth sensor is placed on the bottom of the diamond cell, off center of the symmetry (loading) axis of the cell (more details are provided in the Supplementary Material, *9*).

First motions from >450 acoustic emissions were collected over several experiments up to 26 GPa at 300 K. First motion amplitude varied between 0.3 and 3 mV (corresponding to nanometer-scale displacements) depending on the strength of the acoustic emission and the quality of coupling between the sensors and the diamond cell. First motion durations vary between 1.2 and 1.7 μs, independent of first-motion amplitude; instead, durations appear to be proportional to sample size, indicating our system has high Q factor. First motion duration timescales are consistent with ruptures traversing the (100-150 μm diameter) sample chamber at ~1/3 of shear velocity (~2.2μm/ns in chrysotile at ambient pressure), consistent with theory as well as observations of brittle-like rupture in other systems (*7,10-13*). Signals invariably had 2 or 3 of the traces indicate tensional first motions *(trace moving to positive voltages*), with 1 or 2 of the in-plane traces indicating compressional first motions (*trace moving to negative voltages*).

Compressional and tensional first motions of the sensors are used along with sensor location to determine focal mechanisms (Fig. 4.1). The complexity of the diamond cell, and the

scarcity of sensors necessitates the assumption of double-couple sources, precluding the determination of CLVD components of the focal mechanism (*9*). However, the observed focal mechanisms 1) rule out completely volumetric (i.e., isotropic) sources, and 2) reveal possible relations between slip orientations of sequential events.

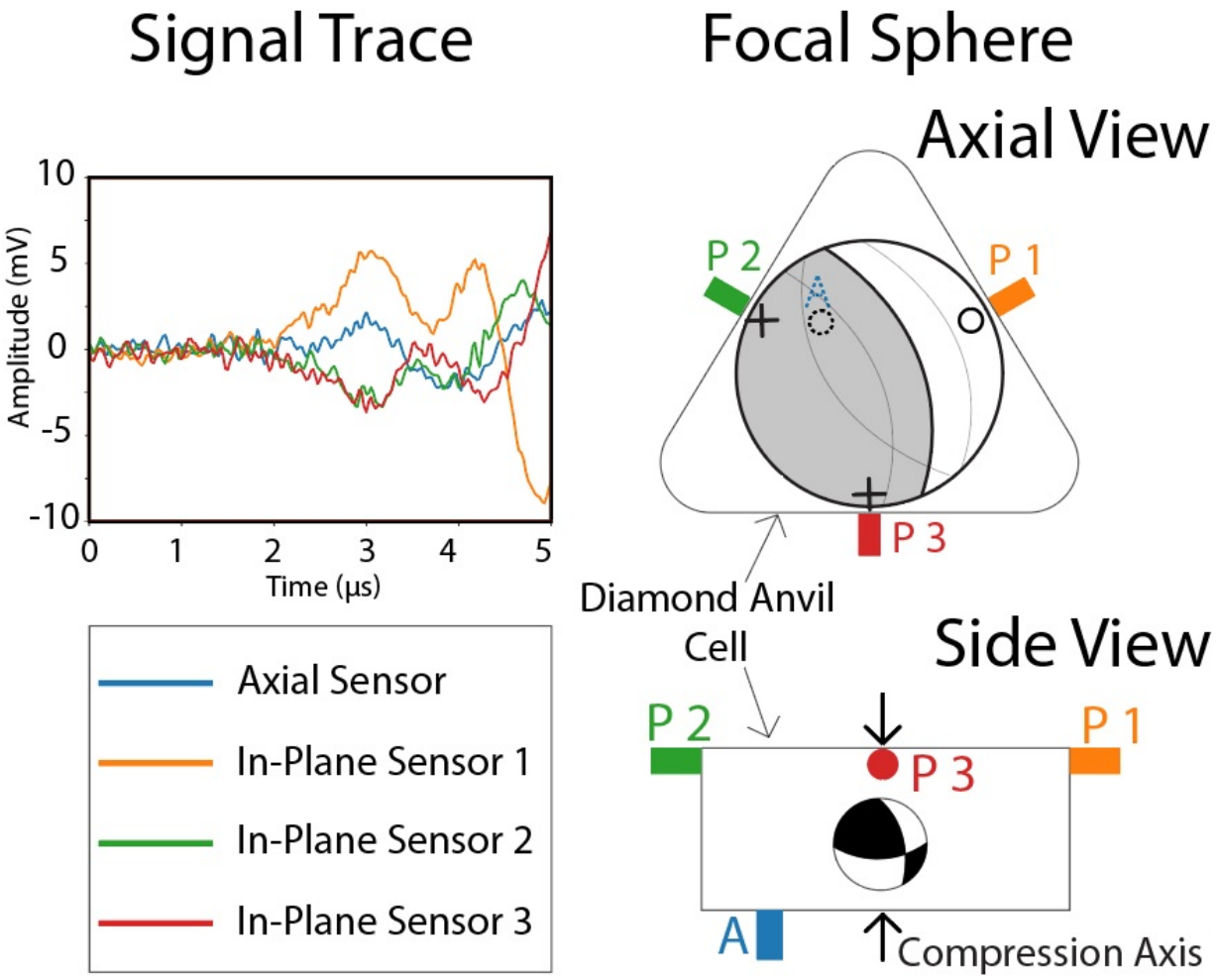

Figure 4.1: Example traces and seismic source diagram for Serpentine at high pressure. *Signal Trace)* An example first motion signal trace is shown. this signal is representative of the average signal quality across our data set. *Focal sphere, Axial View)* Shows a top-down illustration of a focal sphere projection. In-Plane sensors P1,2, & 3 and Axial Sensor A are shown in their relative positions and are color coordinated to the traces they record. All sensors are coupled orthogonally to the triangular pressure cell, with P1, P2, and P3 organized radially, and the Axial sensor attached to the bottom, near the compression axis. The axial sensor and its polarity observation are shown in dashed lines to indicate they are observing from the opposite side of the diamond cell as the In-plane sensors. Each sensor shows a black plus sign if the trace indicated the sample was in compression, and a hollow circle if the trace indicated the sample was in tension. Due to scarcity of sensors, the proposed focal spheres are only roughly constrained, with several degrees of uncertainty in the nodal lines of these spheres. Additional possible nodal lines are shown with thin black lines. *Side View)* An illustrated side view looking along in-plane sensor 3 is shown in the right. An example focal mechanism appropriate for the first motion is shown in the cross sectional plane, approximately in the location of the sample chamber. The axis of compression is shown with black arrows. Additional possible nodal lines are omitted to improve legibility.

Signals were similar enough to allow for sorting into different ‘types’ in all experiments. Cross correlations between signals allowed us to identify five source types, with first motions exhibiting high correlation coefficients (> 95%) that suggest similar slip mechanisms, possibly from a repeating source or a system of related ruptures (*14*). The wavelengths observed here correspond to the resonance of the sample chamber, however, making distinction of rupture zones within the sample chamber beyond the resolution of the present measurements. Correlation between signals of different first motions types, or signals from different experiments, yielded values of 40-80% further confirming that they have different source orientations.

Acoustic emissions appear in clusters, with a typical pressure step yielding several acoustic emissions within 100s of microseconds to seconds of each other. Figure 4.2 shows a subset of our emissions over a ~100 ms timespan, with a mix of first motion types active concurrently, and repetition of first motion types on timescales of ~3-5 ms. Comparison of first motion amplitudes correlates with first motion type, with signals of mutual first motion types tending toward similar amplitudes, indicating that they release similar energy during rupture and suggesting similar rupture area during failure (*9*).

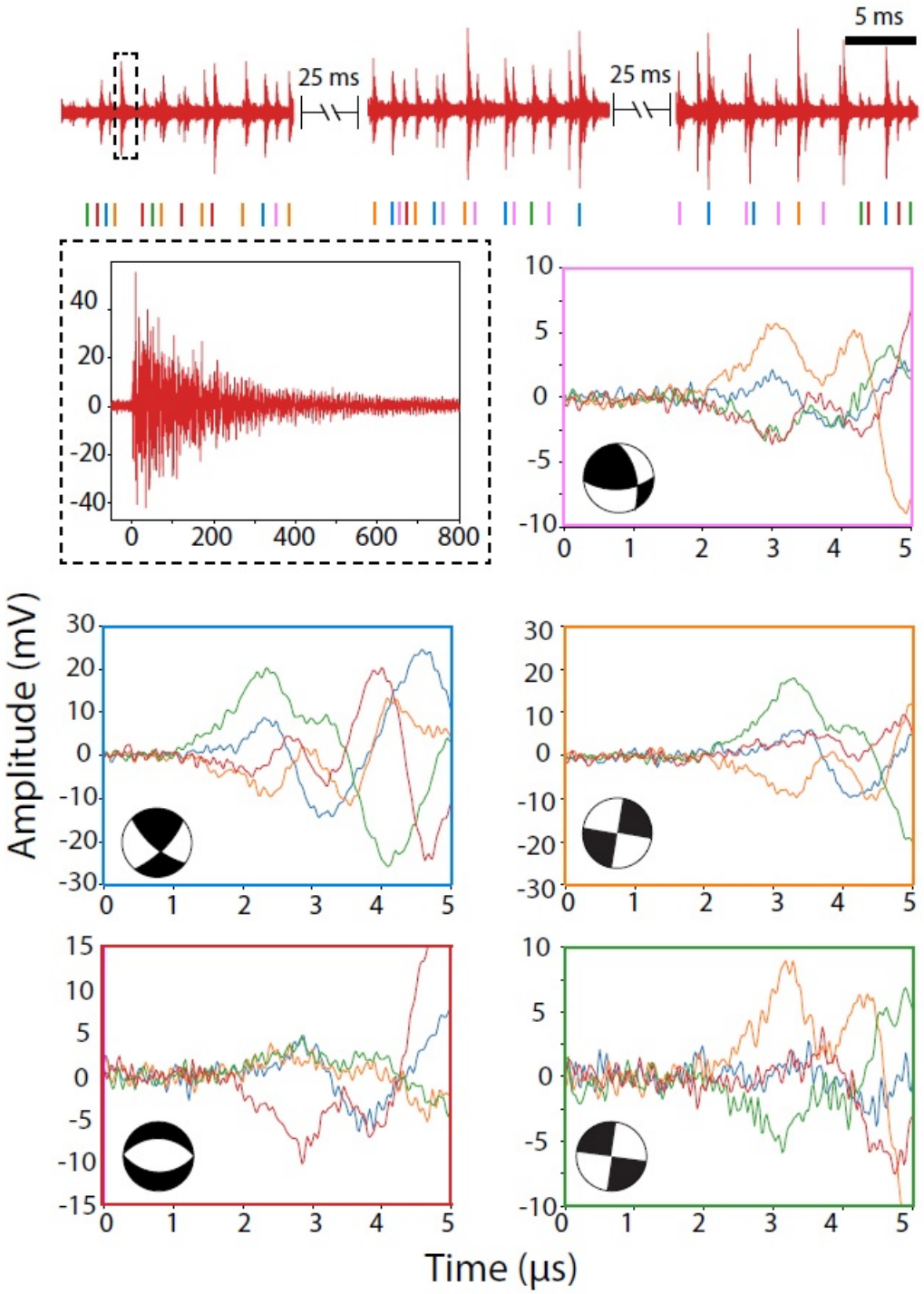

Figure 4.2. Acoustic emission cluster plotted with example first motions. The top shows acoustic emission cluster observed in our most prolific acoustic emission experiment, which yielded 370 emissions at 12 GPa. Each of the three blocks of data are 17.5ms long. Beneath each waveform in the cluster we show a colored bar displaying the first motion type observed for the waveform. Example traces of each of the first motion types are shown color coordinated to the colored bars under the emission cluster. First motions types are shown with their focal mechanisms as inserts as in the side view shown in Figure 4.1. Determination of focal spheres shown here are shown in supplemental figure 4.S1 (*9*). Signals of a given first motion type occur successively with minimum lag times of 3-5 milliseconds. First motions were not discernable for signals with amplitudes too small to distinguish them from background noise or signals that truncated the coda of an earlier signal. A full acoustic waveform is shown in the dashed box and shows the millisecond timescales typical of our signals.

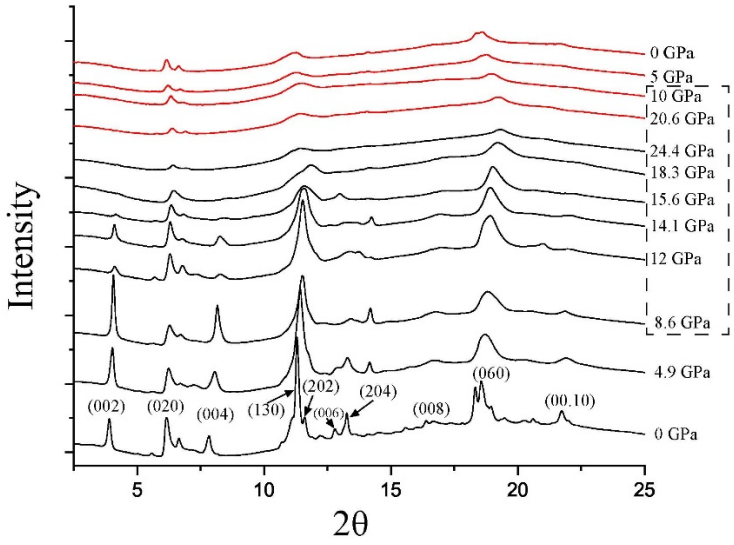

Fig 4.3. X-ray diffraction intensity versus 2 theta for Serpentine on compression and decompression between 0 and 24.4 GPa. The pressure for each diffraction pattern is listed on the right, with pressure steps that yielded acoustic emissions outlined by the dashed box. Patterns taken on decompression are shown in red. Miller indices are shown for the ambient pressure above the ambient pressure diffraction pattern.

Acoustic emissions were collected concurrently with X-ray diffraction on compression between 8 and 24 GPa, and then on decompression, all at 300 K. Diffraction peaks broaden and disappear on compression, demonstrating that the high-pressure transformation of serpentine is solid-state amorphization, with partial re-emergence of several of the diffraction peaks on decompression confirming that there was no melting (Fig. 4.3). Solid-state amorphization is a well-known metastable transformation at high pressures, generally facilitated by shear and often – though not always – reversible (e.g. SiC, $AlPO_4$) (*15-17*). Disappearing diffraction peaks associated with the interlayer spacing between serpentine sheets ([00*l*] peaks), are attributed to the collapse of hydrogen bonds, as seen during the amorphization of other hydrous materials (*18,19*). Re-emerging ([*hk*0]) peaks are associated with the magnesium-silicate sheets, showing that the integrity of the serpentine layers is partially preserved through the amorphization process, and precluding a thermal disordering such as that expected from frictional melting. Amorphization is a crystal-structural instability that can take place on the timescale of acoustic emissions, with subsequent appearance of the equilibrium, crystalline high-pressure phase.

Supplemental Materials

Experimental Methods

We compress natural Serpentine (60% clino- 40% ortho-chrysotile, determined by x-ray diffraction) in diamond anvil cells to 25 GPa and 300K. Spring steel or rhenium gaskets pre-indented to 40-60 μm thick and drilled with holes 100-150 μm in diameter were used in all experiments and samples were prepared following Smart et al. 2019. Pressure was determined using the standard ruby fluorescence technique (*20*).

Acoustic emissions (AE) were recorded with 1-4 Glaser-type conical displacement sensors (model KRNBB-PC) following McLaskey and Glaser (*21*). The sensors have a near-flat frequency response from roughly ~100kHz-5MHz. The built-in preamps were powered with 24VDC, resulting in a sensitivity on the order of 1V/nm when coupled to steel. Signals were digitized at 40MHz using an Elsys TraNET EPC digitizer and TranAX 4.0 recording software. The Merril-Basset DACs often produced highly broadband signals, with signal to noise ratios (SNR) greater than 2 up to the Nyquist frequency of 20MHz and SNR>10 up to 4MHz.

Synchotron X-ray diffraction was performed at beamline 12.2.2 of the Advanced Light Source at Lawrence Berkeley National Laboratory, using an X-ray wavelength of 0.4959 nm, and a distance from the sample to the detector of ~330 cm. Acoustic emissions were collected using the 4-sensor setup described above, though due to portability issues, a Tektronix MSO 2104B Oscilloscope was used instead of the digitizer we used for all other experiments we describe here.

Experiments used 4 acoustic sensors; 3 of these sensors in-plane with each other, located horizontally around the three edges of the upper diamond cell plate, and a fourth sensor was attached from the bottom, off center of the symmetry axis of the diamond cell. A custom clamp was machined from a 2-inch thick polycarbonate plastic cylinder in order to provide an impedance mismatch strong enough to dampen ringing within the system and hold the diamond cells and sensors in place during the acoustic experiments. Acoustic signals arrive simultaneously at the sensors (within ~0.1 μs), indicating that the sensors are acoustically equidistant from the sample chamber within ~0.1mm (wavelengths corresponding to 0.1μs resolution, given wave speeds of mm/μs)

Calibration tests and Control Tests

The diamond anvil cell system is too complex to readily model a waveform arrival from a theoretical source, so we calibrated the sensors using two approaches that provide a known acoustic source for comparison with signals observed from the serpentine samples. Glass capillaries were broken between the diamond anvils used for the high-pressure experiments to ensure that the signals for this calibration use the same ray paths as acoustic emissions produced during the experiment. Pin drop calibrations were performed by dropping a stainless steel 38mm, 0.7mm, diameter sewing needle onto the table of the diamond anvil from a height of 5mm. Pin drop calibrations were performed before and after the collection of acoustic emissions from the sample in order to characterize how effectively the acoustic sensors were coupled to the diamond cell.

Calibration tests give a step-like acoustic pulse, with all traces moving in the same direction, as expected for a single force source transmitted through symmetric paths (*21,22*), confirming that despite the complex geometry and multiple impedance mismatches along the raypath the system maintains the linearity required for first motions analysis of experimental signals. The calibration results also reveal that a useable Greens function cannot be extracted because deconvolution of the calibration source is non-unique, and that a modeling-based determination of the full acoustic response of the diamond cell is beyond the scope of this work. Therefore, we cannot invert for a full moment tensor, thus precluding determination of the CLVD component.

Control tests were performed on our experimental setups to pressures of 30-40 GPa, well beyond the pressure limit of our experiments. We used both spring steel and Rhenium gaskets for these tests, and blank gaskets (with and without holes), 4:1 Methal:ethanol mixture, and $PbCl_2$ as the control test media. Typically, the diamond cell's pressure transmitting screws are equipped with Belleville spring washers in order to control compression. However, when equipped with these springs, rubbing between the washers yielded acoustic signals that triggered our sensors, and therefore Belleville washers were omitted in our experiments. These noise signals are distinguishable from our sample's signals because their frequency content is generally lower (10's-100kHz as opposed to 1-5MHz of the signals from our samples) and they have time delays exceeding a microsecond between the arrivals on different traces. Our sensors are equidistant from the sample chamber, so time delays exceeding ~ 10-20ns (the time it takes a signal to traverse the sample chamber) suggest these signals have sources outside the sample chamber.

Acoustic Waveforms: Figures showing Focal spheres for each acoustic emission type, typical waveforms, and distribution of first motion amplitude vs normalized event number.

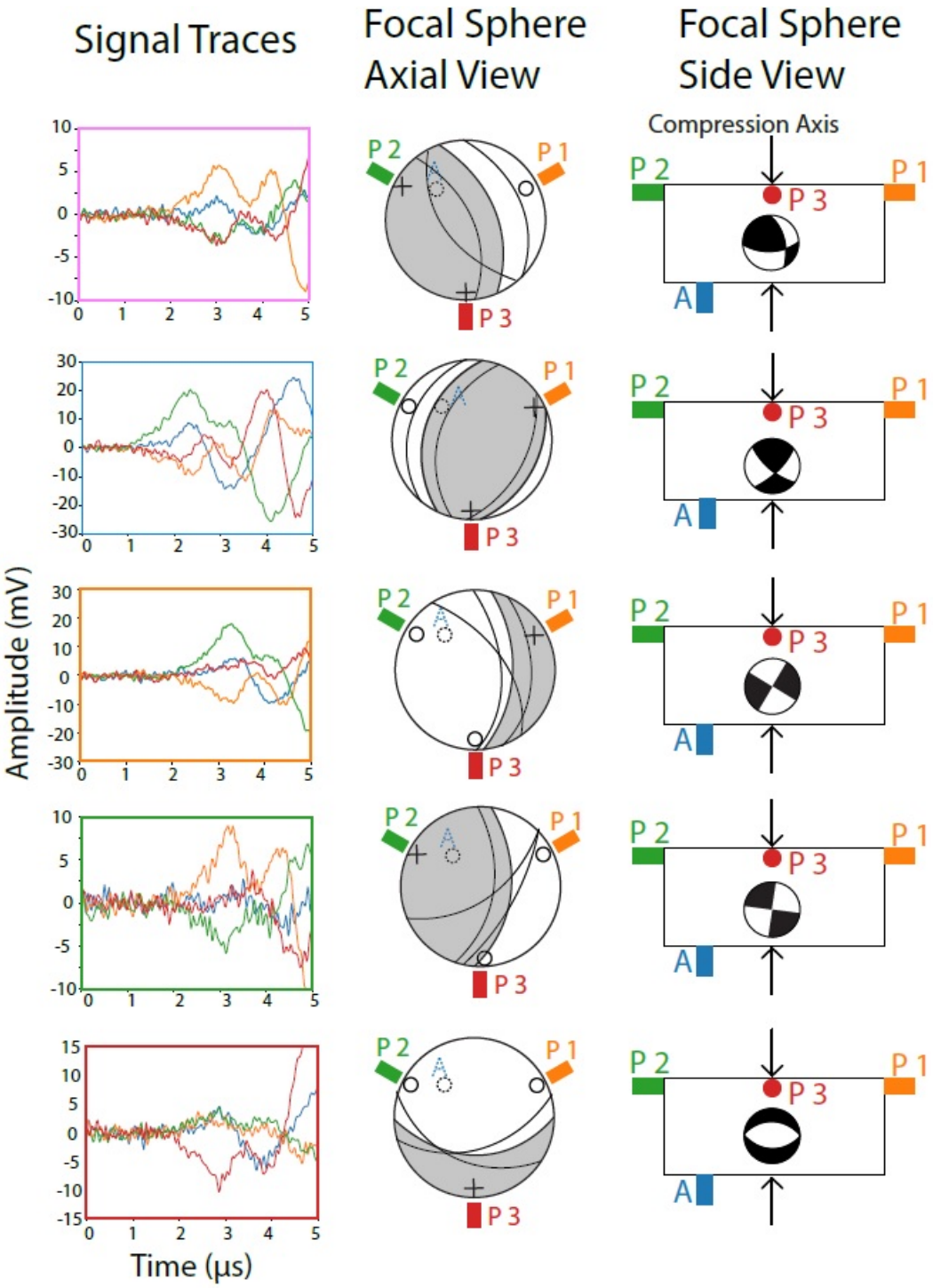

Fig. S1. First motion types with their respective focal spheres are shown. As in Figure 4.1, *Signal Trace*) shows an example first motion signal trace is shown. this signal is representative of the average signal quality across our data set. *Focal sphere, Axial View)* Shows a top-down illustration of a focal sphere projection. In-Plane sensors P1,2, & 3 and Axial Sensor A are shown in their relative positions and are color coordinated to the traces they record. All sensors are coupled orthogonally to the triangular pressure cell, with P1, P2, and P3 organized radially, and the Axial sensor attached to the bottom, near the compression axis. The axial sensor and its polarity observation are shown in dashed lines to indicate they are observing from the opposite side of the diamond cell as the In-plane sensors. Each sensor shows a black plus sign if the trace indicated the sample was in compression, and a hollow circle if the trace indicated the sample was in tension. Due to scarcity of sensors, the proposed focal spheres are only roughly constrained, with several degrees of uncertainty in the nodal lines of these spheres. *Side View)* An illustrated side view looking along in-plane sensor 3 is shown in the right. An example focal mechanism appropriate for the first motion is shown in the cross-sectional plane, approximately in the location of the sample chamber. The axis of compression is shown with black arrows.

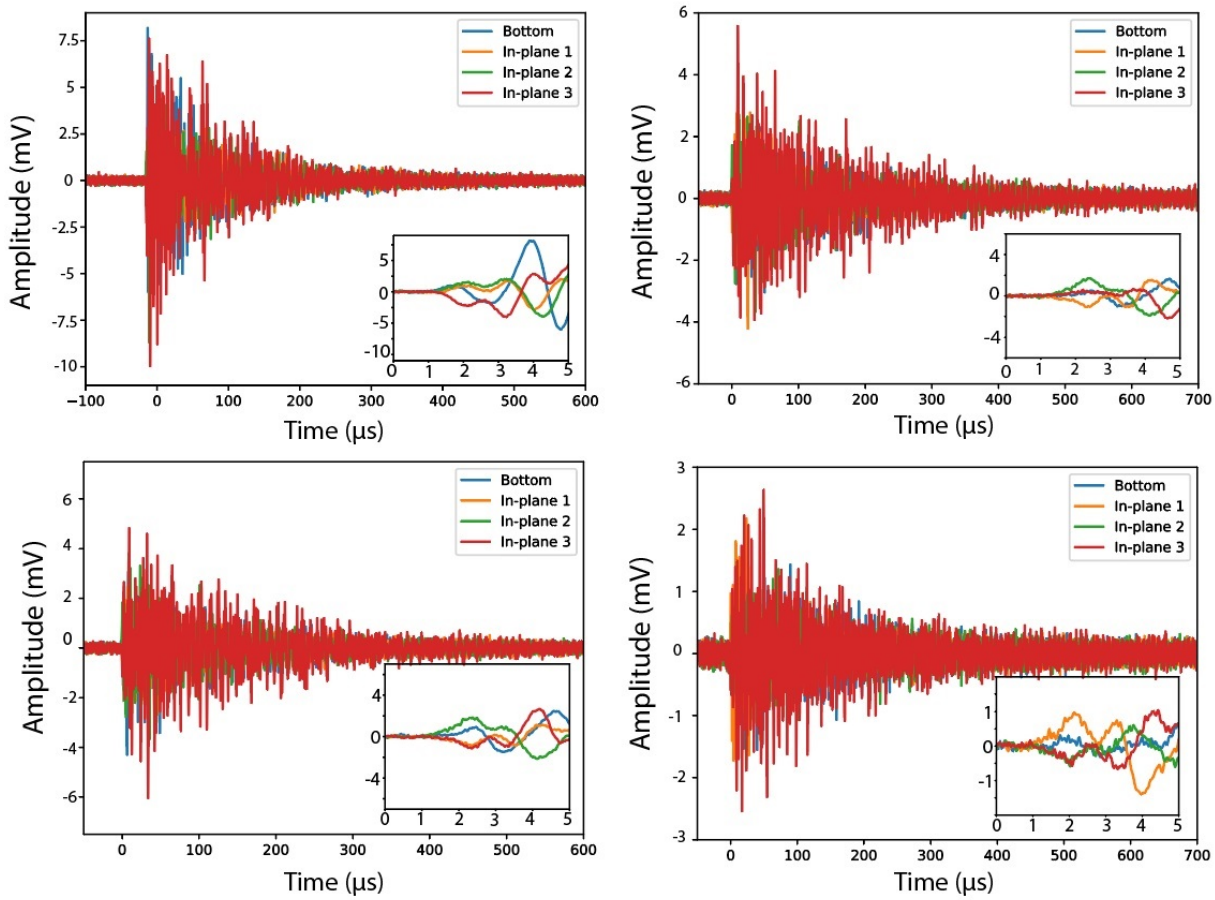

Fig 4.S2. Four example acoustic emission signals and their first motions *(inserts*) are shown. These are 4 signals each with different first-motion character and are average signals that represent the quality of our data well. Duration of the full acoustic waveforms are proportional to first-motion amplitude in all experiments, and vary between 50μs and 1ms, longer than the resonances expected from our sample chamber (~10^{-7}s- 10^{-6}s), though in accord with expected resonance times of the experimental apparatus (Smart et al. 2019, Meade and Jeanloz 1989). Peak waveform amplitudes vary between 1 and 15 mV and durations ranged from 200 to 1000μs.

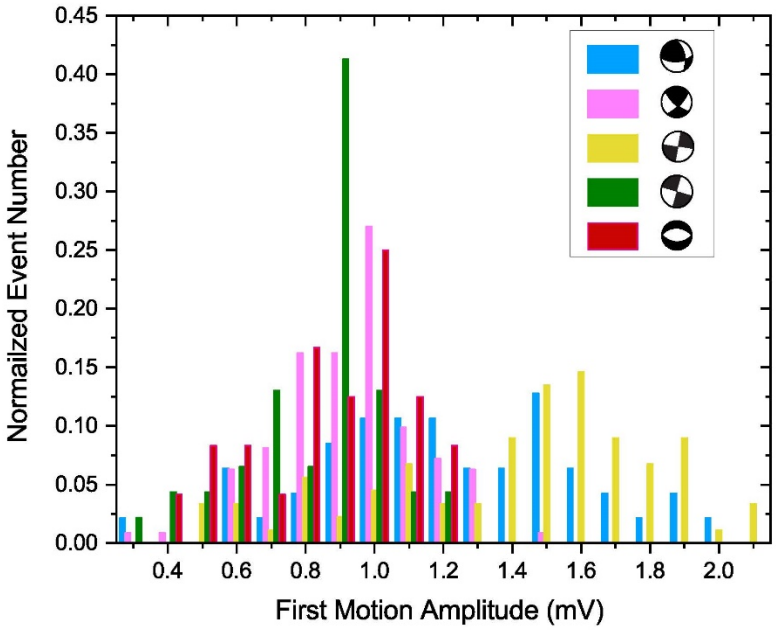

Fig 4.S3. Normalized number of events with a given first motion type are plotted versus first motion amplitude. First motion amplitude in this figure represents the maximum amplitude collected among the 4 sensors for a given signal. Acoustic emissions tallied are the same set shown in figure 4.2. First motions types are color coordinated in the same manner as Figures 4.1 and 4.2, and show the focal mechanisms displayed in figure 1. All emissions were collected from the same sample at the same pressure step, to ensure changes in amplitude are not due to differences in coupling between acoustic sensors and the pressure cell.

Possibilities and limitations for frictional heating during deformation of Serpentine

Though we don't observe evidence of melting, the sample may be transiently heating due to feedback loops between plastic work and rheologic weakening of the material causing localized heating along shear zones (*8,23*). Previous work observed serpentine to remain acoustically active at pressures and temperatures exceeding 25 GPa and 900K, indicating the failure mechanism responsible for acoustic emission is somewhat tolerant of high temperature (*5*). Heat in this case must dissipate quickly enough between successive failures for the serpentine remain solid and regain material strength needed for subsequent failure (*24*). Ambient pressure thermal diffusivity of serpentine (.005-.01 cm^2/s or 0.5-1 $\mu m^2/\mu s$) suggests that it would take ~25-50 μs for heat in the center of the sample to diffuse to the serpentine/diamond interface, where the relatively high mass and heat conductivity of the diamonds act as heat sinks (*25,26*). These 10s of microsecond timescales are easily accommodated within the observed minimum lag time between signals (see Figure 4.2).

While our experiments show that frictional heating is not observed in these laboratory scale experiments, it is possible that melting plays a role when scaled to larger length scales. Figure 4.S4 shows a comparison between the time/distance relations of acoustic transit and thermal diffusion. Acoustic transit times are typically km/s (or μm/ns), while typical thermal diffusivity in rocks is ~1 mm^2/s (1 $\mu m^2/\mu s$). While at shorter length scales, the two curves converge at nm distances and picosecond timescales, at larger distances, acoustic transits are

orders of magnitude faster than thermal diffusion. Therefore, at larger distances, if crystal-structural instability initiates fracture or other rapid deformation in nature, it's possible that frictional heating can then cause melting subsequent to the failure, potentially obscuring the evidence of the initial instability. That is to say, failure due to shear-induced solid-state amorphization and frictional melting are not mutually exclusive. This has bearing not only for faulting at crustal pressures (e.g. generation of pseudotachylites in shear zones) but in deep seismicity as well where localized shear zones generate feedback loops between material strength and frictional heating (and possibly melting) to drive material failure. *(8,27,28)*

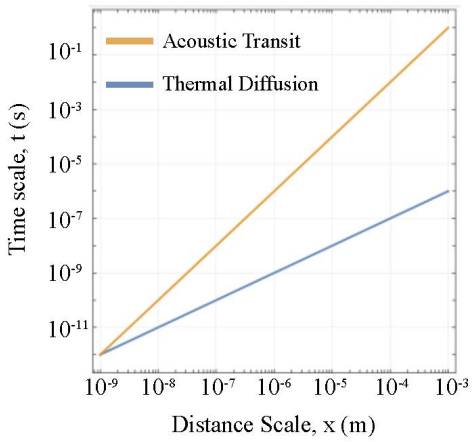

Figure 4.S4. Comparison of the acoustic transit ad thermal diffusion timescales in typical rock, by distance.

References

1. J. Byerlee, FRICTION OF ROCKS. Pure and Applied Geophysics 116, 615-626 (1978).
2. M. S. Paterson and T.-F. Wong, *Experimental Rock Deformation – The Brittle Field*, 2nd Ed.(Springer, New York, 2005) pp 211-237.
3. C. Frohlich, Deep Earthquakes. Deep Earthquakes, 1-574 (2006).
4. S. H. Kirby, W. B. Durham, L. A. Stern, MANTLE PHASE-CHANGES AND DEEP-EARTHQUAKE FAULTING IN SUBDUCTING LITHOSPHERE. Science 252, 216-225 (1991).
5. C. Meade, R. Jeanloz, DEEP-FOCUS EARTHQUAKES AND RECYCLING OF WATER INTO THE EARTHS MANTLE. Science 252, 68-72 (1991).
6. D. P. Dobson, A. A. De Ronde, M. D. Welch, P. G. Meredith, The acoustic emissions signature of a pressure-induced polytypic transformation in chlorite. American Mineralogist 92, 437-440 (2007).
7. A. Schubnel et al., Deep-Focus Earthquake Analogs Recorded at High Pressure and Temperature in the Laboratory. Science 341, 1377-1380 (2013).
8. N. Golding, W. B. Durham, D. J. Prior, L. A. Stern, Plastic Faulting in Ice. Journal of Geophysical Research-Solid Earth 125, 22 (2020).
9. Materials and methods are available as supplementary materials on Science Online.
10. B. Reynard, N. Hilairet, E. Balan, M. Lazzeri, Elasticity of serpentines and extensive serpentinization in subduction zones. Geophysical Research Letters 34, 5 (2007).
11. T. Smart et al., High-pressure nano-seismology: Use of micro-ring resonators for characterizing acoustic emissions. Applied Physics Letters 115, 3 (2019).
12. X. Markenscoff, Cracks as Limits of Eshelby Inclusions. Physical Mesomechanics 22, 42-45 (2019).
13. X. Markenscoff, Self-similarly expanding regions of phase change yield cavitational instabilities and model deep earthquakes. Journal of the Mechanics and Physics of Solids 127, 167-181 (2019).
14. R. M. Nadeau, L. R. Johnson, Seismological studies at Parkfield VI: Moment release rates and estimates of source parameters for small repeating earthquakes. Bulletin of the Seismological Society of America 88, 790-814 (1998).
15. V. I. Levitas, Y. Z. Ma, E. Selvi, J. Z. Wu, J. A. Patten, High-density amorphous phase of silicon carbide obtained under large plastic shear and high pressure. Physical Review B 85, 5 (2012).
16. M. B. Kruger, R. Jeanloz, MEMORY GLASS - AN AMORPHOUS MATERIAL FORMED FROM ALPO4. Science 249, 647-649 (1990).
17. K. J. Kingma, R. J. Hemley, D. R. Veblen, H. K. Mao, HIGH-PRESSURE CRYSTALLINE TRANSFORMATIONS AND AMORPHIZATION IN ALPHA-QUARTZ. High-Pressure Science and Technology - 1993, Pts 1 and 2, 39-42 (1994).18. G. T. Faust, B. Nagy, SERPENTINES - NATURAL MIXTURES OF CHRYSOTILE AND ANTIGORITE. American Mineralogist 41, 817-838 (1956).
19. J. H. Nguyen, M. B. Kruger, R. Jeanloz, Evidence for "partial" (sublattice) amorphization in Co(OH)(2). Physical Review Letters 78, 1936-1939 (1997).
20. A. Dewaele, M. Torrent, P. Loubeyre, M. Mezouar, Compression curves of transition metals in the Mbar range: Experiments and projector augmented-wave calculations. Physical Review B 78, 13 (2008).
21. G. C. McLaskey, S. D. Glaser, Acoustic Emission Sensor Calibration for Absolute Source Measurements. Journal of Nondestructive Evaluation 31, 157-168 (2012).
22. G. C. McLaskey, S. D. Glaser, in Conference on Sensors and Smart Structures Technologies for Civil, Mechanical, and Aerospace Systems 2010. (Spie-Int Soc Optical Engineering, San Diego, CA, 2010), vol. 7647.
23. K. Regenauer-Lieb, D. A. Yuen, Modeling shear zones in geological and planetary sciences: solid- and fluid-thermal-mechanical approaches. Earth-Science Reviews 63, 295-349 (2003).
24. G. C. McLaskey, A. M. Thomas, S. D. Glaser, R. M. Nadeau, Fault healing promotes high-frequency earthquakes in laboratory experiments and on natural faults. Nature 491, 101-U114 (2012).
25. Z. M. Geballe, R. Jeanloz, Origin of temperature plateaus in laser-heated diamond anvil cell experiments. Journal of Applied Physics 111, 15 (2012)
26. P. D. Desal, R. A. Navarro, S. E. Hasan, C. Y. Ho, D. P. DeWitt, T. R. West, Thermophysical properties of selected rocks, Defense Technical Information Center, CINDAS report 23, (1974)
27 H.R. Wenk, Are pseudotachylites products of facture or fusion? Geology, v.6, p507-511 (1978)
28 M. Antolik, D. Dreger, and B. Romanowicz, Finite source study of the great Bolivia earthquake, Geophysical Research Letters, Vol. 23, No. 13, p 1589-1592, (1996)

Chapter 5:

Thoughts on future high-pressure acoustic measurement experiments

As discussed in Chapter 3, there is a problem with the standard practices for acoustic emission (AE) detection in high-pressure experiments. Typical sample sizes range from 100-1000 μm and have sound speeds of ~10 μm/ns, so to capture signals from deformations corresponding to the length of the sample chamber, sampling rates of >0.1-1 GHz are needed. Sampling rates of Piezoelectric detectors most commonly used in high-pressure AE studies range from 2-10 MHZ, with a few reaching as high as 40 MHz. (Green et al. 1993, Incel et al., Dobson et al. Meade and Jeanloz 1989. etc.). Therefore, updated sensors with greater frequency response and sensitivity are crucial.

Whispering Gallery Microsensors (WGM sensors) like the micro-ring resonator presented in Ch. 3 offer a promising solution to this issue, boasting sensitivities as low at ~10 Pa and achieving sampling rates up to the THz range [1- 4]. However, they are currently limited in their utility due to allowing only 1 sensor to be used at once. Subsequent studies should aspire to utilize an array of sensors to enable the characterization of the nano-seismic source. In the following subsection, I cover some of the technical limitations that must be overcome before this method can progress and offer some insights into material choices.

How WGM sensors work:

Whispering Gallery Microsensors are a family of optical detectors with an array of geometries that all operate by measuring modulation of light within a resonator coupled to a fiber optic line. Figure 5.1, after figure 1 in Li et al. [4], shows the Micro Ring resonator presented in Ch. 3, though all WGM sensors operate on the same underlying principles.

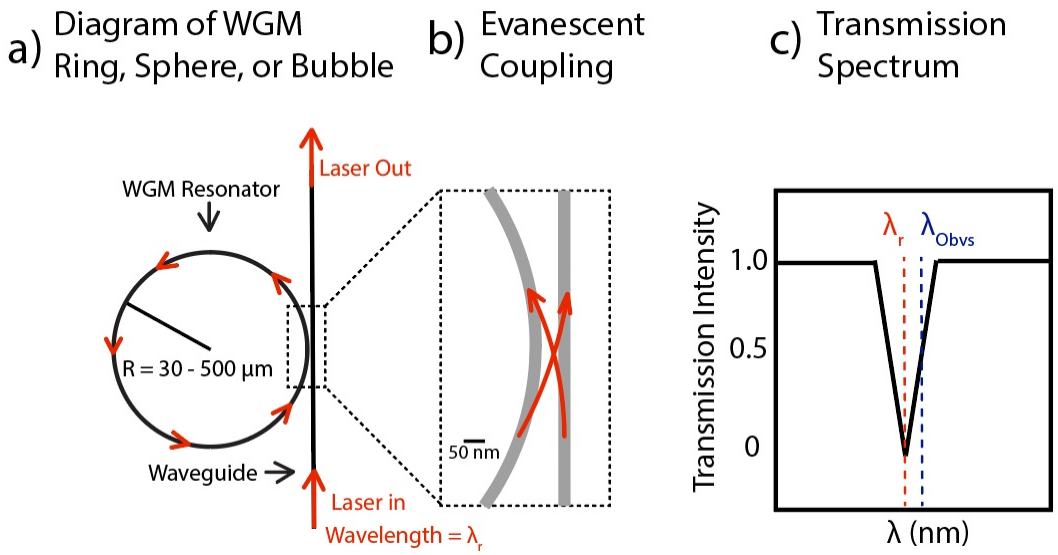

FIG 5.1. After Fig 1 from Li et al. [4]. a) shows the WGM resonator coupled to the fiber optic bus waveguide. b) a close up of the coupling between the waveguide and the WGM resonator. The wavefield intensity decreases exponentially as a function of distance within the fiber, so coupling distance necessarily is on the order of tens of nanometers. The transmission spectrum collected by a downstream detector is shown in c). The dip in the transmission corresponds to resonant wavelength λ_r. Spectrometer measures intensity at λ_{Obvs}, corresponding to the half-width of the dip in intensity.

In detail, the resonator works by evanescent coupling of light between the fiber-optic waveguide and the resonator (Fig 5.1 a). Bus waveguide and resonator are placed a short distance (~50 nm) apart to allow for coupling (Fig 5.1 b). Once inside the resonator, a whispering gallery mode supports resonance of a characteristic resonance wavelength of light, λ_r. This λ_r is determined by the travel-time of light around the ring's circumference, so it is critically dependent on the geometry and index of refraction of the resonator. The change in transmitted intensity is measured at λ_{Obvs}, the half-amplitude of the resonance wavelength, to maximize sensitivity to mode shifts.

When a strain wave passes across the resonator, it deforms the ring, changing the path length and index of refraction, thus shifting the λ_r of the system (Fig 5.1 c). More crucially, the physical oscillation of the ring changes the coupling distance between the ring and the bus waveguide. Wavefield intensity and, therefore, the evanescent coupling is exponentially dependent on distance, so WGM resonators are exceptionally sensitive to deformation.

Factors to Consider when choosing a WGM sensor: Q factor & Resonator Geometry.

The sensitivity of a given WGM sensor is dictated in large part by its ability to retain light energy within its resonator. This property is known as the Quality factor (Q factor) and is characterized by the ratio of light stored to light lost within the resonator. In practice, the Q factor is most critically determined by the smoothness of WGM resonator, since defects or roughness in the surface allow a path for light trapped in the WGM to escape and reduce the strength of the resonance. This loss of light causes the dip in the transmission spectrum to shallow, effectively limiting the response of our sensors (Illustrated in figure 5.2).

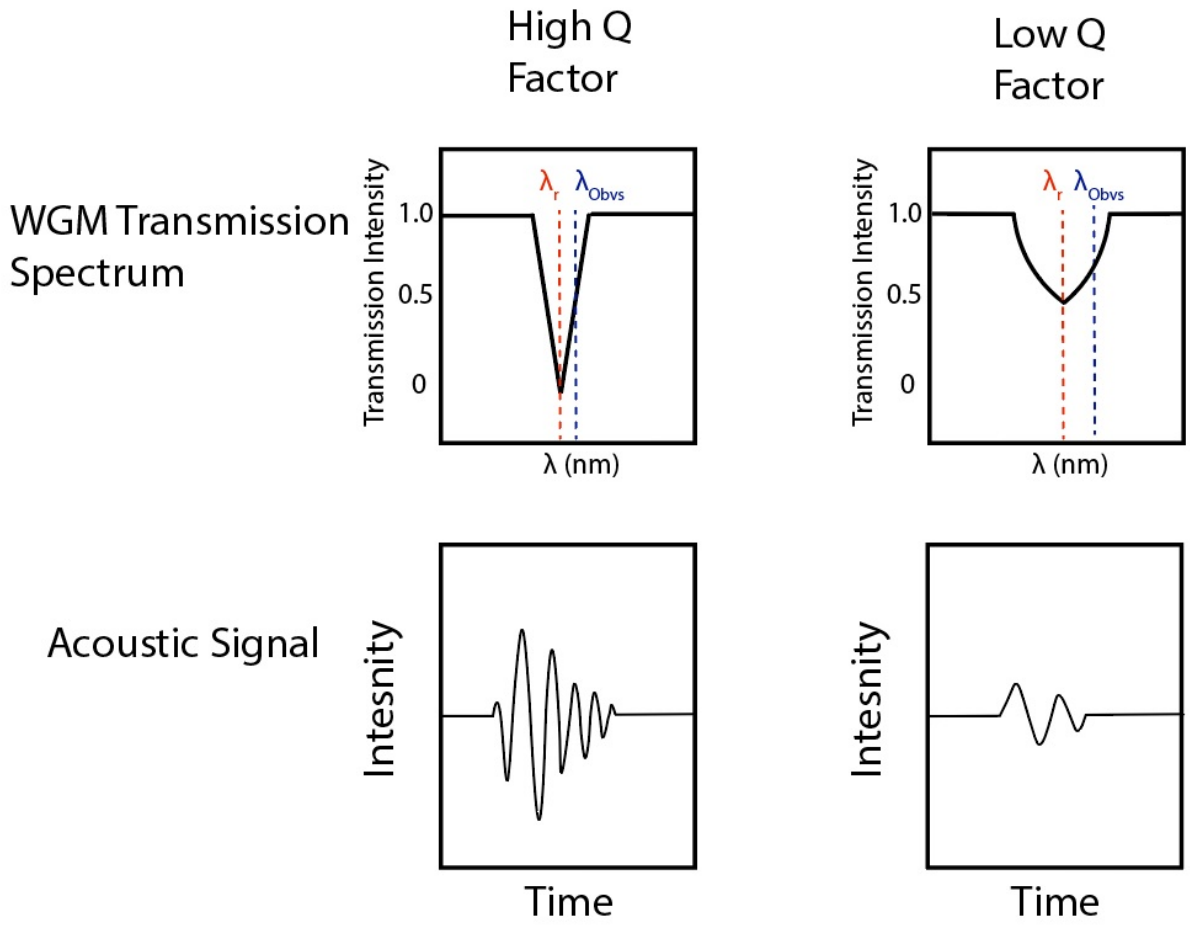

Fig 5.2. Illustration of the effect of the Q factor on the observed signal. Top panels a) and b) show transmission spectra collected from the fiber waveguide after it has coupled with the WGM resonator. λr is the resonant wavelength of the WGM sensor, and λObvs corresponds to the wavelength at which the spectrometer is set to observe. Bottom panels c) and d) show illustrations of acoustic signals collected as a function of time from high and low Q resonators. Note that low Q factor decreases both the sensitivity and frequency response of the WGM resonator.

These resonators can be used to measure a suite of different properties (temperature, pressure, magnetic fields, particles, etc.), which in turn makes them sensitive to many sources of noise [9]. Therefore, choosing the sensor and sensing technique best suited to one's experiment is crucial. The most common geometries for pressure sensing are the Ring Resonator, the Microsphere, and the Microbubble [1-9].

Micro Spheres and Microbubbles are smooth and therefore tend to have high Q factors (10^9-10^{10}) [1,5,6,9]. They are constructed out of stiff materials (generally silica) and therefore change shape less than micro rings, resulting in lower sensitivities, and are larger, with sizes on the scale of mm, which could limit their ability to mechanically resonate at higher frequencies. Spherical resonators are coupled to the sample orthogonally, and therefore could be useful to sense deformation in the coupling direction, but their low angular sensitivity limits their utility. The spherical shape creates practical issues of securing the resonator to the pressure cell and maintaining that connection during the experiment. Capillary sensors present the same issues that Spherical resonators do, and they are most commonly used to sense vibrations while submerged in fluids [1,9]. Of the three, Micro-rings are most readily suited to high-pressure experiments. While typically they have low Q factor (10^4-10^5), new fabrication techniques allow for Q factors

as high as 10^{10} [2-4,9]. Their flat profile allows for easy coupling to the pressure cell, and they can be made from both soft and stiff materials (e.g., plastic, silicon), allowing the designer to tune the parameters more closely to their experimental needs.

Technical Issues with Multi-Channel WGM Acoustic sensing:

Equipment:

Laser Source: the mode-locking technique described above requires a narrowband laser tuned at λr, to excite the resonance of the WGM most strongly. With multiple sensors, this becomes difficult, since microscopic differences in the manufacture of the WGM sensor results in a unique λr for each resonator. Using a broadband laser could excite many resonators simultaneously, though because the laser wavelength would be tuned to an average λ, there would be a drop in sensitivity and increased noise.

Spectrometer and Oscilloscope: While it has been demonstrated that one can sense multiple rings with a single channel spectrometer [8], tracking more than three resonators would prove difficult due to the overlap in resonances during AE detection. Characterization of signals from multiple resonators would, therefore, be more straightforward if collected using a multi-channel spectrometer. The resolution of the spectrometer would ideally be < 0.2nm, as the transmission dip resulting from the resonance of the WGM is on that order. The oscilloscope in a multi-sensor array would each need to accept at least 4 but ideally 16 or more channels with sampling rates of > GHz.

Calibration of the Sensor:

While WGM sensors have been used in a variety of experiments to sense pressure, further work is needed to characterize a nano-seismic source fully. This can be accomplished using known acoustic sources, such as ball drops and capillary breaks described by McLaskey and Glaser [10], or in using a pulse laser focused on a fluid medium to cause vibration as described in [3]. The distance response of Micro-ring resonators has been simulated and characterized by Zhang et al. [11], though live tests of AE from off-axis angles still need to be performed.

Due to the nature of the evanescent coupling, the WGM sensor is especially sensitive to pressure waves that alter the distance between the resonator and the bus waveguide. When a compressional wave traverses the resonator, the resonator will deform (degree of deformation determined by Poisson's ratio). The initial deformation of the WGM relative to the waveguide, and thus the acoustic first motions depend on the direction the compressional wave is traveling to the sensor (figure 5.4). Because the acoustic sensors are fixed in place during the experiment, the direction in which first motions traverse the WGM sensor is also fixed, and it should be possible to extract first motion data from nano-seismic events similar to work presented in Chapter 4, provided that a calibration source is well characterized.

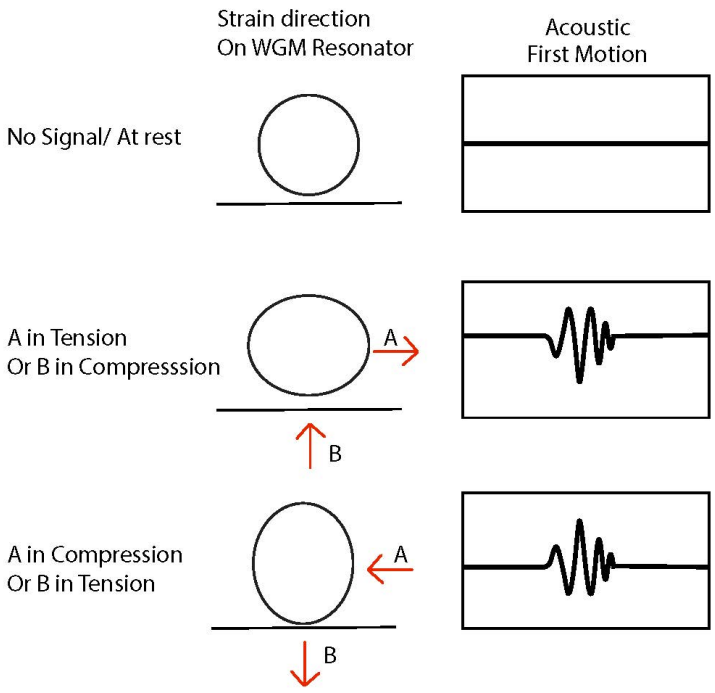

Figure 5.4: Illustration of Acoustic first motions as determined by deformation of WGM resonator caused by compressional waves.

References

1. D. W. Vogt, R. Leonhardt, Terahertz whispering gallery mode bubble resonator. Optica 4, 809-812 (2017).
2. B. Q. Dong, C. Sun, H. F. Zhang, Optical Detection of Ultrasound in Photoacoustic Imaging. Ieee Transactions on Biomedical Engineering 64, 4-15 (2017).
3 B. Q. Dong et al., Isometric multimodal photoacoustic microscopy based on optically transparent micro-ring ultrasonic detection. Optica 2, 169-176 (2015).
4. H. Li, B. Q. Dong, Z. Zhang, H. F. Zhang, C. Sun, A transparent broadband ultrasonic detector based on an optical micro-ring resonator for photoacoustic microscopy. Scientific Reports 4, 8 (2014).
5. T. Ioppolo, M. I. Kozhevnikov, V. Stepaniuk, M. V. Otugen, V. Sheverev, Micro-optical force sensor concept based on whispering gallery mode resonators. Applied Optics 47, 3009-3014 (2008).
6. T. Ioppolo, M. V. Otugen, Pressure tuning of whispering gallery mode resonators. Journal of the Optical Society of America B-Optical Physics 24, 2721-2726 (2007).
7. R. Madugani, Y. Yang, V. H. Le, J. M. Ward, S. N. Chormaic, Linear Laser Tuning Using a Pressure-Sensitive Microbubble Resonator. Ieee Photonics Technology Letters 28, 1134-1137 (2016).
8. H. M. Wei, S. Krishnaswamy, Polymer micro-ring resonator integrated with a fiber ring laser for ultrasound detection. Optics Letters 42, 2655-2658 (2017).
9. X. Jiang, A. J. Qavi, S. H. Huang & L. Yang, 'Whispering gallery microsensors: a review', arXiv:1805.00062 (2018)
10. G. C. McLaskey, S. D. Glaser, Acoustic Emission Sensor Calibration for Absolute Source Measurements. Journal of Nondestructive Evaluation 31, 157-168 (2012).
11. Z. Zhang et al., Theoretical and experimental studies of distance dependent response of micro-ring resonator-based ultrasonic detectors for photoacoustic microscopy. Journal of Applied Physics 116, 8 (2014).